Available on the CERN CDS information server

CMS PAS SMP-20-010

CMS Physics Analysis Summary

Contact: cms-pag-conveners-smp@cern.ch

2021/03/31

Study of quark and gluon jet substructure in dijet and Z+jet events from pp collisions

The CMS Collaboration

Abstract

A measurement of jet substructure observables describing the distribution of particles within quark- and gluon-initiated jets is presented in this note. Proton-proton collision data at $\sqrt{s} = 13$ TeV collected by the CMS detector are used, corresponding to an integrated luminosity of 35.9 fb^{-1}. A set of generalized angularities with varying sensitivity to the distributions of transverse momenta and angular distances within a jet are studied. The analysis is carried out using a dijet event sample enriched in gluon-initiated jets, and, for the first time, also a Z+jet event sample enriched in quark-initiated jets. The measurement is carried out in bins of jet transverse momentum, and as a function of jet size parameter, for multiple observables with and without a jet grooming procedure applied. Using these measurements, the ability of various models to describe jet substructure observables is studied, showing the clear need for improvements in Monte Carlo generators.

Contents

1 Introduction

Interactions between quarks and gluons, commonly referred to as partons, are governed by quantum chromodynamics (QCD), which confines carriers of the strong interaction charge (colour) inside colourless hadrons. When quarks or gluons are produced by collisions in particle colliders, collimated showers of hadrons are formed, screening the strong charge. Theoretical calculations and experimental methods cluster such showers into jets using dedicated clustering algorithms [1] that allow for the correlation of the kinematic properties of the jets with those of the produced partons. Furthermore, the study of the distribution of particles within a jet, the jet substructure, can be analysed to determine the likelihood that a jet originates from a quark or from a gluon. Heavy, boosted particles or resonances that decay to quarks, i.e. top quarks, and W, Z, and Higgs bosons, have characteristic distributions of jet substructure observables; several algorithms have been developed to distinguish such jets from those originating from single partons [2–4]. These techniques are used in numerous measurements and searches at the LHC, and would therefore benefit from a better understanding and simulation of jet substructure observables.

Jets originating from single quarks, called quark jets in the following, and those arising from single gluons, similarly called gluon jets, are known to differ in their make-up. At leading order (LO) in perturbative QCD, the difference in Casimir colour factor between quarks ($C_{\mathrm{F}} = 4/3$) and gluons ($C_{\mathrm{A}} = 3$) leads to differences in the probability to radiate a soft gluon, which are proportional to the ratio $C_{\mathrm{A}}/C_{\mathrm{F}} = 9/4$ [5]. We therefore expect gluon jets on average to contain more constituents, with a wider geometric spread in the detector [6–11]. However, there are also a variety of other non-perturbative effects that determine the jet substructure, including modelling of the hadronization and colour reconnection, which are typically described by phenomenological models in Monte Carlo (MC) event generators. The description of jet fragmentation and substructure thus requires a combined understanding of perturbative calculations and non-perturbative effects. While the description of jets initiated by quarks is better constrained by many previous measurements, the modelling of gluon jets is less well understood [12].

Previous measurements of observables sensitive to the jet fragmentation at the LHC have been carried out by the ATLAS [13–19], CMS [20–24], ALICE [25, 26], and LHCb [27] Collaborations. Jet substructure observables for the separation of jets initiated by quark, gluons, W, Z, and Higgs bosons, and top quarks have been measured by ATLAS [28–38] and CMS [39–43]. While previous measurements have concentrated on specific observables, final states, or regions of phase space, the goal of this measurement is to systematically explore multiple dimensions of phase space and observable definitions. As outlined in Ref. [12], multiple aspects of MC event simulation models of jet substructure can be tested with such a comprehensive set of measurements.

In this note, we report on a measurement of a set of five observables that distinguish quark- and gluon- initiated jets, the generalized angularities λ^{κ}_{β} [44]. These observables have previously been used by the CMS [45, 46] and ATLAS [47] Collaborations to discriminate between quark and gluon jets. We measure these observables in quark- and gluon-jet enriched Z+jet and dijet event samples, respectively. In the Z+jet sample, we study a jet recoiling against a Z boson decaying to a pair of muons. Within the dijet event sample, we separately measure the distributions for the more central (smaller absolute rapidity $|y|$) of the two jets, and the more forward (larger $|y|$) of the two jets. The sample of the more central jet is predicted to provide a higher purity of gluon jets. Each observable is measured as a function of jet transverse momentum p_{T}, with different jet size parameters, and with and without applying a jet grooming procedure [48] that removes soft and wide-angle radiation from the jet. The detector-level distributions are unfolded to particle-level for each configuration and observable and normalized to unity in each p_T bin.

2 The CMS detector and event reconstruction

The central feature of the CMS apparatus is a superconducting solenoid of 6 m internal diameter, providing a magnetic field of 3.8 T. Within the solenoid volume are a silicon pixel and strip tracker, a lead tungstate crystal electromagnetic calorimeter (ECAL), and a brass and scintillator hadron calorimeter (HCAL), each composed of a barrel and two endcap sections. Forward calorimeters extend the pseudorapidity coverage provided by the barrel and endcap detectors. Muons are detected in gas-ionization chambers embedded in the steel flux-return yoke outside the solenoid.

A more detailed description of the CMS detector, together with a definition of the coordinate system used and the relevant kinematic variables, can be found in Ref. [49].

The global event reconstruction (also called particle-flow event reconstruction [50]) aims to reconstruct and identify each individual particle in an event, with an optimized combination of all subdetector information. In this process, the identification of the particle type (photon, electron, muon, charged hadron, neutral hadron) plays an important role in the determination of the particle direction and energy. Photons (e.g. coming from π^0 decays or from electron bremsstrahlung) are identified as ECAL energy clusters not linked to the extrapolation of any charged particle trajectory to the ECAL. Electrons (e.g. coming from photon conversions in the tracker material or from semileptonic B hadron decays) are identified as a primary charged particle track, and potentially many ECAL energy clusters. These clusters correspond to the extrapolation of the track to the ECAL, and to possible additional bremsstrahlung photons emitted along the way through the tracker material. Muons (e.g. from B hadron semileptonic decays) are identified as tracks in the central tracker consistent with either a track or several hits in the muon system, and associated with calorimeter deposits compatible with the muon hypothesis. Charged hadrons are identified as charged particle tracks neither identified as electrons, nor as muons. Finally, neutral hadrons are identified as HCAL energy clusters not linked to any charged hadron trajectory, or as a combined ECAL and HCAL energy excess with respect to the expected charged hadron energy deposit.

The silicon tracker measures charged particles within the pseudorapidity range $|\eta| < 2.5$. It consists of 1440 silicon pixel and 15 148 silicon strip detector modules. For nonisolated particles of $1 < p_T < 10$ GeV and $|\eta| < 1.4$, the track resolutions are typically 1.5% in p_T and 25–90 (45–150) μm in the transverse (longitudinal) impact parameter [51].

The candidate vertex with the largest value of summed physics-object p_T^2 is taken to be the primary pp interaction vertex. The physics objects are jets, clustered using the anti-k_T jet finding algorithm [52, 53] with the tracks assigned to candidate vertices as inputs, and the associated missing transverse momentum, taken as the negative vector sum of the p_T of those jets.

The energy of photons is obtained from the ECAL measurement. The energy of electrons is determined from a combination of the track momentum at the main interaction vertex, the corresponding ECAL cluster energy, and the energy sum of all bremsstrahlung photons attached to the track. The energy of muons is obtained from the corresponding track momentum. The energy of charged hadrons is determined from a combination of the track momentum and the corresponding ECAL and HCAL energies, corrected for the response function of the calorimeters to hadronic showers. Finally, the energy of neutral hadrons is obtained from the corresponding corrected ECAL and HCAL energies.

In the barrel section of the ECAL, an energy resolution of about 1% is achieved for unconverted or late-converting photons in the tens of GeV energy range. The remaining barrel photons have a resolution of about 1.3% up to a pseudorapidity of $|\eta| = 1$, rising to about 2.5% at $|\eta| = 1.4$. In the endcaps, the resolution of unconverted or late-converting photons is about 2.5%, while the remaining endcap photons have a resolution between 3 and 4% [54].

For each event, hadronic jets are clustered from these reconstructed particles using the infrared and collinear safe anti-k_{T} algorithm [52, 53] with distance parameters of 0.4 and 0.8, referred to as AK4 and AK8 jets in the following. Jet momentum is determined as the vectorial sum of all particle momenta in the jet, and whose magnitude is found from simulation to be, on average, within 5 to 10% of the magnitude of the true momentum over the whole p_{T} spectrum and detector acceptance. Additional proton-proton interactions within the same or nearby bunch crossings (pileup) can contribute additional tracks and calorimetric energy depositions to the jet momentum.

The pileup per particle identification (PUPPI) algorithm [55, 56] is used to mitigate the effect of pileup at the reconstructed particle level, making use of the local momentum distribution, event pileup properties and tracking information. Charged particles identified to be originating from pileup vertices are discarded. For each neutral particle, a momentum distribution variable is computed using the surrounding charged particles compatible with the primary vertex within the tracker acceptance ($|\eta| < 2.5$), and using both charged and neutral particles in the region outside of the tracker coverage. The momenta of the neutral particles are then rescaled according to their probability to originate from the primary interaction vertex deduced from the momentum distribution variable, superseding the need for jet-based pileup corrections [55].

Jet energy corrections are derived from simulation to bring the measured response of jets to that of particle level jets on average. In situ measurements of the momentum balance in dijet, photon + jet, Z + jet, and multijet events are used to account for any residual differences in jet energy scale in experimental data and simulation [57]. The jet energy resolution amounts typically to 15% at 10 GeV, 8% at 100 GeV, and 4% at 1 TeV. Additional selection criteria are applied to each jet to remove jets potentially dominated by anomalous contributions from various subdetector components or reconstruction failures.

Events of interest are selected using a two-tiered trigger system [58]. The first level (L1), composed of custom hardware processors, uses information from the calorimeters and muon detectors to select events at a rate of around 100 kHz within a time interval of less than 4 μs. The second level, known as the high-level trigger (HLT), consists of a farm of processors running a version of the full event reconstruction software optimized for fast processing, and reduces the event rate to around 1 kHz before data storage.

3 Data and simulated samples

This analysis is based on pp collision data collected by the CMS experiment in 2016 at a centre-of-mass energy of $\sqrt{s} = 13$ TeV, corresponding to an integrated luminosity of 35.9 fb^{-1} and with an average of 23 pileup interactions. Events are selected online using multiple sets of trigger paths. The Z+jet candidate events are collected with a trigger requiring at least one isolated muon with $p_{\mathrm{T}} > 24$ GeV and $|\eta| < 2.4$, with an efficiency to select an event with at least one muon exceeding 90% [59]. Dijet events with high p_{T} jets are collected with triggers requiring at least one AK4 or AK8 jet above a certain threshold in p_T with an efficiency exceeding 99%. Apart from the trigger with the highest p_T threshold of 450 GeV, the triggers are prescaled, i.e. only a fraction of the collision data events passing the trigger are saved, resulting in a lower integrated luminosity for these paths. Dijet events with jet p_T below the lowest p_T threshold are collected with a zero bias trigger that randomly selects a fraction of the collision events. Table 1 summarises the zero bias and jet triggers with their integrated luminosity and the offline p_T bin thresholds for which the triggers are used.

Table 1: Summary of zero bias and jet triggers used in the analysis for the dijet region. For each trigger, the integrated luminosity and number of events collected by it are given. The offline p_T bin threshold(s) indicate the lower edge of the p_T bin(s) measured with data from a given trigger.

Online p_T threshold	Integrated luminosity	Offline p_T bin threshold(s)	Number of events
0 (zero bias)	2.90×10^{-5} fb^{-1}	50 GeV	309512
40 GeV	2.64×10^{-4} fb^{-1}	65 GeV	446183
60 GeV	7.19×10^{-4} fb^{-1}	88 GeV	387849
80 GeV	2.73×10^{-3} fb^{-1}	120, 150 GeV	757778
140 GeV	2.39×10^{-2} fb^{-1}	186 GeV	1014702
200 GeV	1.03×10^{-1} fb^{-1}	254 GeV	841507
260 GeV	5.88×10^{-1} fb^{-1}	326 GeV	1821727
320 GeV	1.75 fb^{-1}	408 GeV	1918614
400 GeV	5.14 fb^{-1}	481 GeV	1960323
450 GeV	35.9 fb^{-1}	614, 800, 1000 GeV	6421782

The processes of interest in this analysis are Z boson production in association with jets, and events uniquely composed of jets produced through the strong interaction (QCD multijet production). Their simulation is performed with multiple combinations of MC event generators to estimate the detector response and systematic uncertainties. The Z boson production in association with jets is simulated at leading-order (LO) with the MADGRAPH5_aMC@NLO v2.2.2 [60] generator with up to four outgoing partons in the matrix element, and showered with PYTHIA v8.212 [61] using the Lund string fragmentation model [62, 63] for jets, interfaced using the MLM merging scheme [64]. This sample is hereafter referred to by MG5+PYTHIA8. The PYTHIA8 parameters for the underlying event are set according to the CUETP8M1 tune [65, 66]. A second Z+jet sample is generated with HERWIG++ v2.7.1 [67, 68] in standalone mode with the UE-EE-5C underlying event tune [69] to assess systematic uncertainties related to the modelling of the parton showering and hadronization. This sample has one outgoing parton in the matrix element, recoiling against the Z boson. The MADGRAPH5_aMC@NLO and HERWIG++ samples are normalized to the NNLO (QCD) + NLO (EW) cross sections [70].

The QCD multijet production is simulated separately with two different generator configurations: MADGRAPH5_aMC@NLO combined with PYTHIA8, and HERWIG++ in standalone mode. In the former sample, again referred to by MG5+PYTHIA8, up to four outgoing partons are allowed in the matrix element. It is again interfaced to the parton shower using the MLM merging scheme, and the CUETP8M1 tune is also used for the underlying event parameters. In the standalone HERWIG++ sample, the matrix element has two outgoing partons, and the same underlying event tune is used as in the HERWIG++ Z+jet sample. The LO NNPDF 3.0 [71] parton distribution functions (PDFs) with $\alpha_S(m_Z) = 0.130$ are used in all generated samples. Backgrounds from top quark-antiquark pair production, W boson production in association with jets, as well as diboson production, have been estimated to contribute less than 1% to the analysis phase space.

All generated samples are passed through a detailed simulation of the CMS detector using GEANT4 [72]. To simulate the effect of additional pp collisions within the same or adjacent bunch crossings, additional inelastic events are generated using PYTHIA8 and superimposed on the hard-scattering events. The MC simulated events are scaled to reproduce the distribution of the number of interactions observed in the experimental data. The MG5+PYTHIA8 and HERWIG++ simulations have additional selection requirements to ensure that the energy scale of the generated hard scattering process is greater than those of the overlapping pileup events. Because of their stochastic nature, this can affect the MC p_T distribution slope at low p_T, within the total MC uncertainty; however, this has a negligible effect on the unfolded results and uncertainties.

Additional samples of Z boson production in association with jets and QCD multijet production, without detector simulation, are compared to the unfolded experimental data distributions. Predictions are computed at LO with PYTHIA v8.243 with the CP2 and CP5 tunes [73], HERWIG v7.1.4 [74] at LO with angular-ordered showering and the CH3 tune [75], and with SHERPA v2.2.10 [76–78] at LO, and also with two (one) extra jets for QCD multijet (Z+jet) production with CKWW matching [79–81].

As discussed in Refs. [39, 73, 75, 82], the choice of $\alpha_S(m_Z)$ used in the final-state shower evolution in MC event generators has a significant impact on the shape of jet substructure observables for quark and gluon jets. While the MG5+PYTHIA8, HERWIG++, and PYTHIA8 CP2 predictions use larger values of $\alpha_S(m_Z)$ for the final state showering of 0.1383, 0.127, and 0.130, respectively, the PYTHIA8 CP5, HERWIG CH3, and SHERPA predictions all use a common value of 0.118.

4 Event selection

The measurement is carried out using two event samples: a Z+jet sample that is enriched in quark jets, and a dijet sample that is enriched in gluon jets. The Z+jet selection requires at least two reconstructed muons with $p_T > 26\,\text{GeV}$ to guarantee a trigger efficiency exceeding 99%. A Z boson candidate is reconstructed from two oppositely-charged muons with $|\eta| < 2.4$ and a dimuon invariant mass within 20 GeV of the Z boson mass. At least one reconstructed jet with $p_T > 30\,\text{GeV}$ and $|y| < 1.7$ that does not overlap with the muons of the Z boson candidate is required. The requirement on jet rapidity ensures that jets are fully reconstructed within the tracker coverage. The Z boson candidate, with transverse momentum p_T^Z, and the jet with largest p_T, with transverse momentum $p_T^{j_1}$, are required to have a transverse momentum asymmetry $|p_T^{j_1} - p_T^Z|/(p_T^{j_1} + p_T^Z) < 0.3$, and an azimuthal separation larger than 2 radians. The requirements on momentum asymmetry and azimuthal separation are introduced to restrict the measurement to a phase-space dominated by interactions where a single parton is emitted in the hard scattering process. The substructure of this jet is measured.

The dijet selection requires at least two reconstructed jets with $p_T > 30\,\text{GeV}$ and $|y| < 1.7$. The two jets with largest transverse momentum, $p_T^{j_{1,2}}$, are required to have a transverse momentum asymmetry $|p_T^{j_1} - p_T^{j_2}|/(p_T^{j_1} + p_T^{j_2}) < 0.3$, and an azimuthal separation larger than 2 radians. The substructure of these two jets is measured. In the following, the jet with smaller $|y|$ is labelled as the central jet, whilst the jet with larger $|y|$ is labelled as the forward jet.

Table 2 summarises the selection criteria of the Z+jet and dijet event samples. The detector-level distributions are unfolded to particle-level, i.e. only considering final state particles after hadronization with proper lifetime $c\tau > 10\,\text{mm}$. At particle-level the same selection criteria are applied to muons and particle-level jets, with the exception of the jet p_T threshold that is lowered to 15 GeV. Whilst the detector resolution of jet $|y|$ and ϕ, as well as that of the muon p_T, is small enough to maintain equivalent particle- and detector-level selection criteria, the resolution of jet p_T is significantly larger. The particle-level jet p_T threshold is therefore lowered to avoid biasing the detector-level phase space. We note that muons at particle-level are not "dressed", i.e. radiated photons are not considered part of the muon, since this has a negligible effect on the muons.

Table 2: Summary of the selection criteria for the Z+jet and dijet event samples.

Sample	Event selection
Z+jet	$\geq$2 muons with $|\eta| < 2.4$ and $p_T^{\mu} > 26$ GeV
	Opposite charge muons
	$|m_{\mu\mu} - m_Z| < 20$ GeV
	$\geq$1 jet with $|y| < 1.7$ and $p_T^{j} > 30$ GeV,
	not overlapping with muons of the Z boson candidate
	$\Delta\phi(j_1, Z) > 2$
	$|p_T^{j_1} - p_T^{Z}|/(p_T^{j_1} + p_T^{Z}) < 0.3$
Dijet (central and forward)	$\geq$2 jets with $|y| < 1.7$ and $p_T^{j} > 30$ GeV
	$\Delta\phi(j_1, j_2) > 2$
	$|p_T^{j_1} - p_T^{j_2}|/(p_T^{j_1} + p_T^{j_2}) < 0.3$

We quantify the fraction of quark and gluon jets in these event samples using the MG5+PYTHIA8 simulation. As discussed in [12], there is no unique way of defining a quark or gluon jet, and our choice of approach is as follows. The parton from which a jet originates is obtained by first clustering jets from all generated partons (from the matrix element and the shower up to hadronization) together with the generated final-state particles, where the four-momenta of the generated partons are scaled by a very small number. The jets clustered in this way are almost identical to those clustered without generator partons because the added partons, with extremely small energy, do not affect the clustered jet momentum. The quark or gluon with highest p_T in the jet then defines the origin of the jet. Figure 1 shows the resulting gluon fractions of the Z+jet, and central and forward dijet AK4 jets as a function of p_T. The Z+jet sample is enriched in quark jets, making up 64–76% of the jets in the sample. The central and forward dijet jets are dominated by 69–72% gluon jets at low p_T, and by 55–68% quark jets at high p_T. The central dijet jets have a consistently higher fraction of gluon jets than the forward dijet jets across the whole p_T range.

Quark jets are typically considered to be those jets initiated by light-flavour quarks (u, d, s). However, our Z+jet sample also has a small contribution from jets initiated by heavy-flavour quarks (b, c), whose behaviour was measured in [39], and is in between that of light-flavour quark jets and gluon jets. Their presence will therefore lessen the expected differences between light-flavour quark jets and gluon jets.

The p_T distribution in CMS data and simulation for the Z+jet and central dijet AK4 jets is shown in Fig. 2. The data distribution in bins of p_T collected by prescaled triggers (see Table 1) is multiplied by the corresponding prescale factors to reproduce the smoothly-falling physical spectrum. The data distribution is compared to predictions from two generator configurations, where the total number of events in the simulations has been scaled to match that in the data distribution. In both selection regions, the MG5+PYTHIA8 simulation provides a better description of the experimental data. MG5+PYTHIA8 is therefore used to estimate the detector response consistently in both samples in this note, while HERWIG++ is used to evaluate

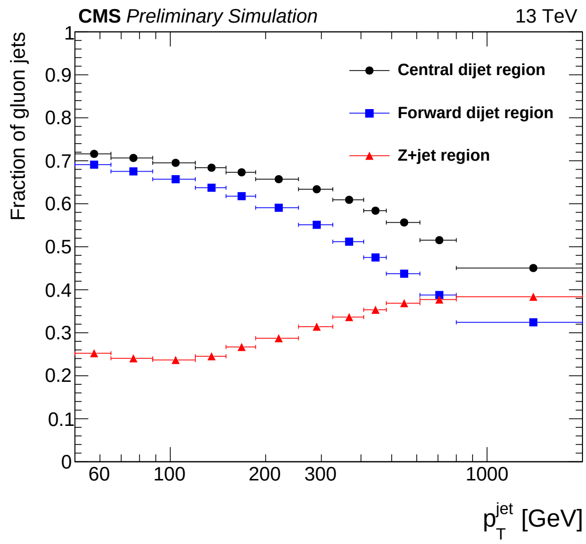

Figure 1: Fraction of AK4 gluon jets in the Z+jet region (red triangles), and the central (black circles) and forward (blue squares) jets in the dijet region.

systematic uncertainties.

5 Jet substructure observables

For the AK4 and AK8 jets of interest we compute and measure a set of jet substructure observables with discrimination power to separate quark and gluon jets. The generalized angularities [44] are defined as:

$$\lambda_{\beta}^{\kappa} = \sum_{\mathrm{i}\in\mathrm{jet}} z_{\mathrm{i}}^{\kappa} \left(\frac{\Delta R_{\mathrm{i}}}{R}\right)^{\beta}, \tag{1}$$

where z_{i} is the fractional transverse momentum carried by the ith jet constituent, R is the jet size parameter, and ΔR_{i} is the displacement of the constituent from the jet axis, defined as $\Delta R_{\mathrm{i}} = \sqrt{(\Delta y_{\mathrm{i}})^2 + (\Delta\phi_{\mathrm{i}})^2}$ where Δy_{i} and $\Delta\phi_{\mathrm{i}}$ are the separations in rapidity and azimuthal angle, respectively, between the jet axis and the i^{th} constituent. The parameters $\kappa \geq 0$ and $\beta \geq 0$ control the momentum and angular contributions, respectively. For $\beta > 1$, the anti-k_{T} jet axis is used to calculate ΔR. For $\beta \leq 1$, ΔR is calculated using the jet axis constructed by the winner-takes-all (WTA) method [83]. The use of the WTA axis significantly simplifies theoretical calculations of these observables, while for observables with $\beta > 1$ computation is feasible with both axis definitions. However, using the anti-k_{T} jet axis results in an observable that is more akin to the jet mass [40]. To calculate the WTA axis, the constituents of the anti-k_{T} jet are reclustered using the p_{T}-based WTA scheme. The resultant jet has the (y, ϕ) of the constituent with the largest p_{T}.

The five observables measured in this note are Les Houches angularity (LHA) $= \lambda_{0.5}^{1}$ [84], width $= \lambda_{1}^{1}$, thrust $= \lambda_{2}^{1}$ [85] , multiplicity $= \lambda_{0}^{0}$, and $(p_{\mathrm{T}}^{D})^2 = \lambda_{0}^{2}$. These are shown in Fig. 3 as points in the (κ, β) plane. Of these variables, only LHA, width, and thrust are infrared and collinear (IRC) safe as a result of having $\kappa = 1$ [83]. However, multiplicity and $(p_{\mathrm{T}}^{D})^2$ have been widely used for quark and gluon discrimination [45, 46]. The calculation of multiplicity only includes constituents with $p_{\mathrm{T}} > 1\,\mathrm{GeV}$, at both detector- and particle-level. Each of the observables is designed to emphasise a particular feature of the jet. The LHA, width, and

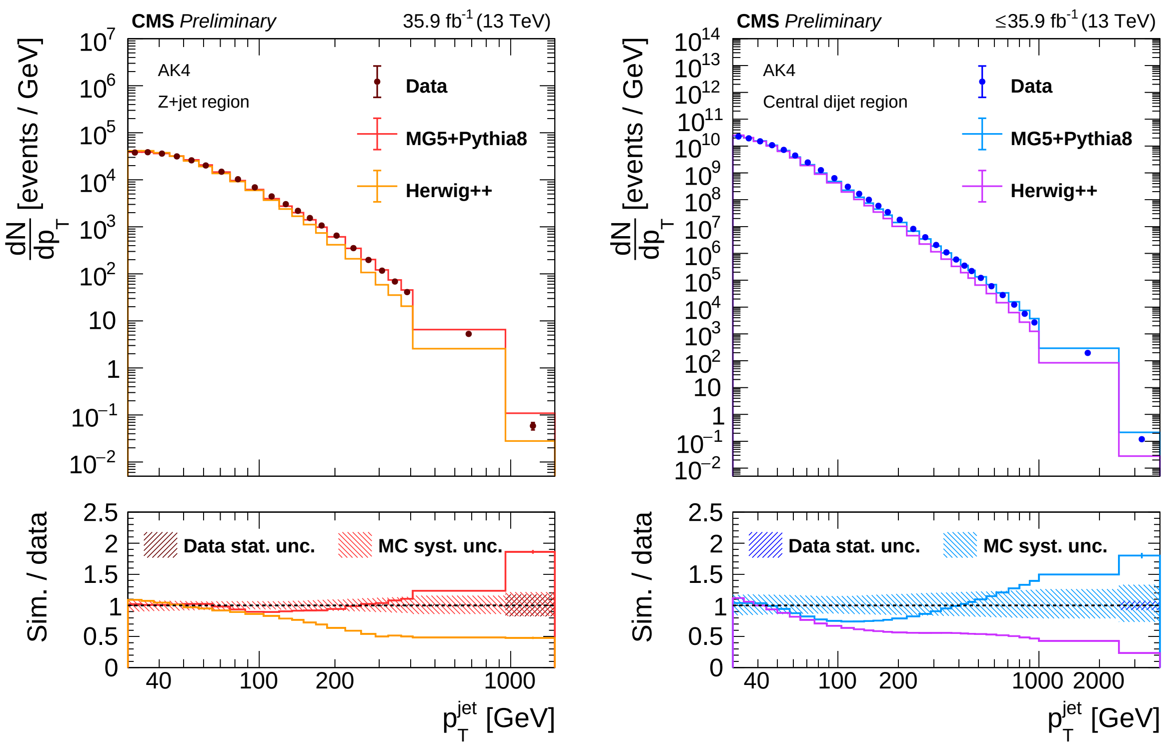

Figure 2: Data to simulation comparisons of the jet p_{T} in the Z+jet (left) and central dijet (right) regions. The error bars correspond to the statistical uncertainties of the experimental data. The darker hashed region in each ratio plot indicates the statistical uncertainty in the experimental data, whilst the lighter hashed region represents the total uncertainty in the MC prediction. This includes all experimental, physics modelling, scale, and PDF uncertainties described in Section 6.

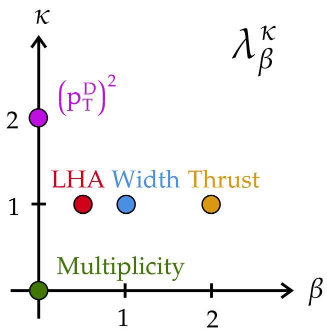

Figure 3: The five generalized angularities λ_β^κ used in this analysis, represented in the (κ, β) plane. The Les Houches Angularity is denoted by LHA. Adapted from [44].

thrust observables take into account both the momentum fraction and the angular distribution of constituents within the jet. Since the weighting of the latter contribution differs across these variables, comparing them can highlight differences in constituent positions within the jet. We expect gluon jets to have, on average, larger values of these observables due to the larger number of constituents that are further from the jet axis. In contrast, $(p_T^D)^2$ places more value on those higher-momentum constituents, irrespective of their position in the jet. With gluon jets typically having more lower-momentum constituents, we therefore expect them to generally have smaller values of $(p_T^D)^2$. While the three IRC-safe angularities are particularly sensitive to the modelling of perturbative emissions in jets, the other two have larger contributions from non-perturbative effects and are thus subject to larger uncertainties in their predictions and measurements.

In this note, we measure each substructure observable with various configurations. Each observable is computed in multiple bins of p_T, and for two different jet size parameters, $R = 0.4$ and 0.8. For each observable, we further calculate a variant where the observables are computed on the jet clustered with the anti-k_T algorithm from only those charged constituents of the original jet ("charged-only"). While observables computed with both charged and neutral constituents can be described more easily from first-principle calculations, the charged-only variants can be measured with a better resolution as a result of the high efficiency and precision of the tracking detector.

Further, we compute a groomed variant of each observable, where the jet is reclustered with the Cambridge–Aachen (CA) algorithm [86], and then groomed using the modified mass-drop algorithm [87, 88], known as the *soft drop* algorithm [48]. This splits the jet into two subjets by undoing the last step of the CA jet clustering. It regards the jet as the final soft drop jet if the two subjets satisfy the condition:

$$\frac{\min(p_T^{(1)}, p_T^{(2)})}{p_T^{(1)} + p_T^{(2)}} > z_{\text{cut}} \left(\frac{\Delta R_{12}}{R} \right)^{\beta_{\text{sd}}}, \tag{2}$$

where $p_T^{(1)}$ and $p_T^{(2)}$ are the transverse momenta of the two subjets, R is the size parameter of the jet, $\Delta R_{12} = \sqrt{(\Delta y_{12})^2 + (\Delta\phi_{12})^2}$ is the distance between the two subjets, and z_{cut} and β_{sd} are tunable parameters of soft drop, set to $z_{\text{cut}} = 0.1$ and $\beta_{\text{sd}} = 0$ in this study. If the condition is not met, the declustering procedure is repeated with the subjet that has the larger p_T of the two, and the other subjet is rejected. This grooming procedure removes soft and wide-angle radiation from the jet, thereby making the jet substructure observables more resilient to effects from pileup, underlying event, and initial-state radiation. Note that in all cases, the jet p_T used for binning is taken from the original ungroomed anti-k_{T} jet (i.e. using charged+neutral constituents, before calculating the WTA axis, and before grooming). A summary of all variations of the observables measured in this note is given in Table 3.

Table 3: Summary of the variants of observables measured in this note.

Dimension	Variants
Region	Z+jet vs. central dijet vs. forward dijet
Observable λ_{β}^{κ}	LHA, width, thrust, multiplicity, $(p_{\mathrm{T}}^{D})^2$
Jet p_{T}	$50 < p_{\mathrm{T}} < 65\,\mathrm{GeV}$, ..., $p_{\mathrm{T}} > 1000\,\mathrm{GeV}$
Jet size parameter R	0.4 vs. 0.8
Constituents	Charged+neutral vs. charged-only
Grooming	Ungroomed vs. groomed

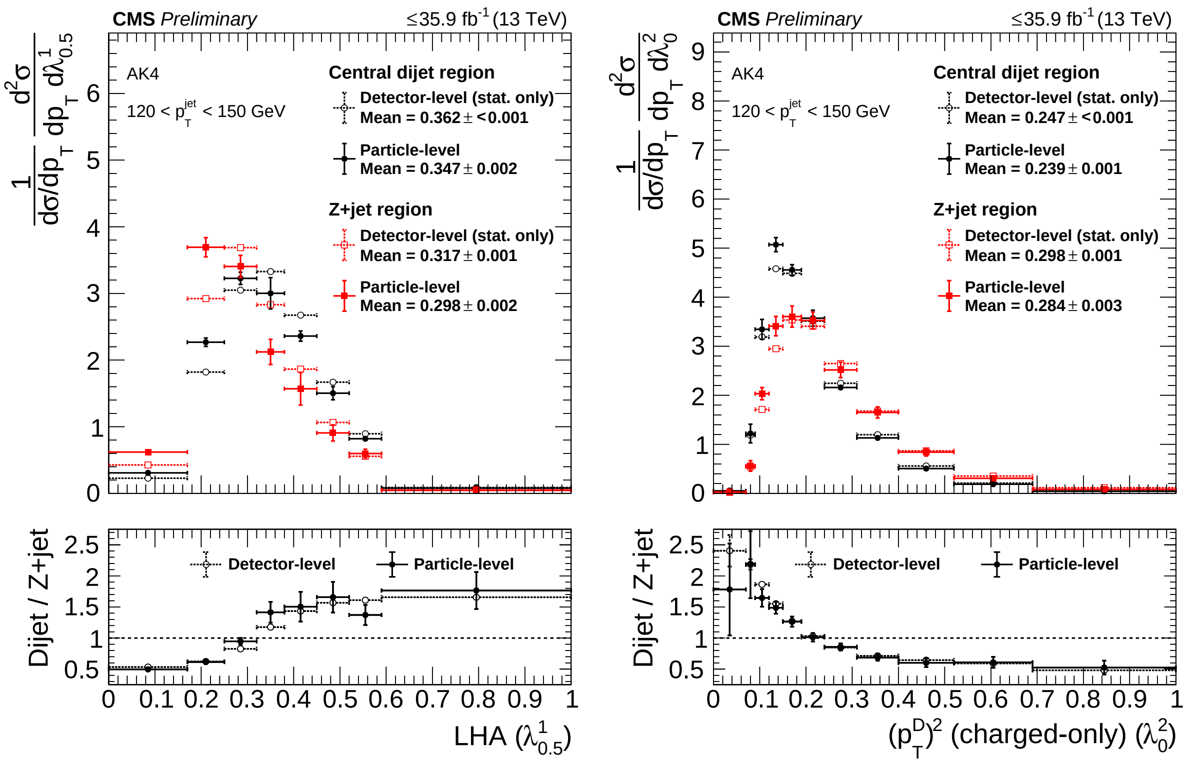

Figure 4: Detector-level and particle-level (unfolded) experimental data distributions of LHA ($\lambda_{0.5}^{1}$) (left) using charged+neutral constituents, and $(p_{\mathrm{T}}^{D})^2$ (λ_{0}^{2}) (right) using only charged constituents, for jets with $120 < p_{\mathrm{T}} < 150$ GeV in the Z+jet (red) and central dijet (black) regions. The detector-level data uncertainties are purely statistical. The particle-level (unfolded) data uncertainties include systematic uncertainties. Also shown is the mean of each distribution, calculated from the binned distribution. The ratio plots show the ratio of dijet to Z+jet distributions, for both the detector- and particle-level distributions.

Figure 4 shows the distributions of two representative jet substructure observables in experimental data, computed from AK4 jets with $120 < p_{\mathrm{T}} < 150$ GeV in the central dijet and Z+jet regions, at both detector- and particle-level. The discrimination power between quark and gluon jets for each observable can be deduced by comparing the distributions in the Z+jet and central dijet regions that are enriched in quark and gluon jets, respectively. As previously mentioned, gluon jets exhibit on average larger values of LHA, width, thrust, and multiplicity, and smaller values of $(p_{\mathrm{T}}^{D})^2$, than quark jets. The distortion of the distribution by detector effects can also be inferred by comparing the detector-level data distributions with their corresponding particle-level (unfolded) data distributions (further explained in Section 6). The charged-only $(p_{\mathrm{T}}^{D})^2$ (Fig. 4, right) is an example where the difference between detector-level data and particle-level (unfolded) data is small as a result of only considering charged constituents. To aid comparison, the mean of each distribution is quoted. The mean is computed from the binned distribution, which is an approximation to the real mean of the underlying distribution, treating experimental data and simulation consistently, both at detector- and particle-level. While the uncertainty quoted for the mean in detector-level data is purely statistical, the uncertainty quoted for the mean in particle-level (unfolded) data also includes systematic uncertainties (further explained in Section 6).

6 Unfolding and systematic uncertainties

The experimental data distributions are unfolded to particle-level using unregularized unfolding as implemented in the TUNFOLD package [89]. The particle level distribution and covariance matrix are obtained by minimizing $\chi^2 = (y - Ax)^T V_{yy}^{-1} (y - Ax)$, where A is the particle-to-reconstructed phase space migration matrix, V_{yy} is an estimate of the covariance of the observations y, and x is an estimator of the true particle-level values. The migration matrix in the 2D phase space of $(p_{\mathrm{T}}, \lambda_{\beta}^{\kappa})$ is derived from the MG5+PYTHIA8 simulation, matching particle-level jets with detector-level jets by requiring an angular separation of half the jet size parameter. Before the detector-level distribution is unfolded, background from “fakes”, i.e. jets that pass the reconstruction criteria, but fail the particle-level selection, are subtracted. The proportion of fakes ranges from <10% for jets at 50 GeV to <1% at 1 TeV. The contribution from other standard model processes was found to be negligible. The migration matrix also takes into account those particle-level jets that fail the reconstruction criteria, to correct for the reconstruction inefficiency.

The binning of the migration matrix takes into account the resolution of the observables. We define purity as the fraction of reconstructed events that are generated in the same $(p_{\mathrm{T}}, \lambda_{\beta}^{\kappa})$ bin, and stability as the fraction of generated events that are reconstructed in the same bin. Both quantities are $\geq$50% in most bins. The detector-level bins have half the width of the particle-level bins in both p_{T} and λ_{β}^{κ}, to guarantee an over-constrained system for the minimisation carried out during unfolding.

Various sources of systematic uncertainty are considered, which are treated as uncorrelated among each other, but correlated in the $(p_{\mathrm{T}}, \lambda_{\beta}^{\kappa})$ plane. These are divided into experimental sources, uncertainties related to the physics model used to derive the migration matrix, and inherent unfolding uncertainties. Experimental and physics model uncertainties are treated by constructing variations in the migration matrix, and propagating the changes to the final unfolded 1D distribution.

Uncertainties in the calibration of the jet energy scale (JES) and jet energy resolution (JER) measurement [57] are taken into account by varying the jet p_{T} when constructing the migration matrix. Furthermore, we account for variations in the measurement of the particle-flow candidates, which are propagated to the computation of jet substructure observables in the migration matrix. These include variations of the charged hadron momentum scale by $\pm$1%, photon energy scale by $\pm$1%, and neutral hadron energy scale by $\pm$3% [50, 57]. Finally, we estimate the uncertainty in jet p_{T} and substructure observables related to pileup by reweighting the simulated events within the uncertainty of the pileup distribution. For the Z+jet region, this corresponds to a $\pm$4.6% shift in the minimum-bias cross section, whilst for the dijet region it is a +4.6/-13.8% shift to account for larger variations from the use of prescaled triggers. Note that no uncertainty related to the integrated luminosity is considered as this only affects the overall normalization and therefore does not affect the normalized distributions presented in this note. Uncertainties on the muon reconstruction and identification are significantly smaller than the aforementioned uncertainties, and are therefore not included.

Uncertainties due the choices of the renormalization and factorization scales (μ_F, μ_R) are computed from the envelope of six variations by factors (1/2, 1/2), (1/2,1), (1,1/2), (2,2), (2,1) and (1,2) [90, 91]. The uncertainty from the PDFs is determined using the LO NNPDF set, where the root-mean-square of 100 pseudo-experiments provided by the PDF set represents the uncertainty envelope. For the MG5+PYTHIA8 prediction, these uncertainties related to scale choices and PDFs mainly vary the prediction of jet momenta, while the substructure observables are only mildly modified. The uncertainty in the modelling of the parton shower and hadronization process is estimated using HERWIG++ to construct an alternative response matrix. This uncertainty is treated as single-sided when building the covariance matrix, since the experimental data distributions are generally found to be enveloped by the MG5+PYTHIA8 and HERWIG++ predictions. It was tested that rescaling the p_T spectrum of the HERWIG++ prediction to match that of the MG5+PYTHIA8 prediction does not significantly change the estimated uncertainty size, confirming that this uncertainty mainly captures differences in the shower and hadronization modelling of substructure rather than the modelling of the p_T spectrum.

The unfolding procedure reproduces the particle-level distributions when unfolding a statistically-independent sample from the same generator that is used to derive the response matrix. The statistical uncertainty of the simulation that is used to derive the migration matrix is propagated through the unfolding and results in a contribution to the covariance matrix. The statistical uncertainties in the presented distributions correspond to those of the input experimental data, while statistical uncertainties in the response matrix are considered as part of the systematic uncertainties.

Figure 5 shows the size of the considered uncertainties in the ungroomed LHA ($\lambda^1_{0.5}$) for AK4 jets with $120 < p_T < 150$ GeV in the central dijet region before (left) and after (right) the distribution for the given p_T bin is normalized. While the JES uncertainty has the largest effect in the yield variations due to migration across the jet p_T boundaries, it plays a limited role for the normalized jet substructure distributions, where the shower and hadronization model uncertainty is typically dominant.

7 Results and discussion

Experimental data distributions unfolded to particle level in the Z+jet and central dijet regions are presented in Figs. 6-10 for the ungroomed substructure observables of AK4 jets with $120 < p_T < 150$ GeV. As a simple quantitative assessment of agreement of each generator prediction with CMS data, values of χ^2/N_{bins} are quoted, where N_{bins} is the number of bins of the distribution. The χ^2/N_{bins} is computed taking into account the covariance matrix including all statistical and systematic uncertainties. The agreement of the simulation with the experimental data varies depending on the observable and sample. In the Z+jet region, MG5+PYTHIA8 provides the best description of all observables. HERWIG++ typically predicts smaller values of all observables, except $(p_T^D)^2$ for which it predicts larger values than MG5+PYTHIA8. In the central dijet region, the agreement of both generators is worse than in the Z+jet region. HERWIG++ shows a slightly better description of the experimental data than MG5+PYTHIA8, except for multiplicity and $(p_T^D)^2$. In both Z+jet and central dijet regions, the MG5+PYTHIA8 and HERWIG++ predictions tend to envelope the experimental data distributions.

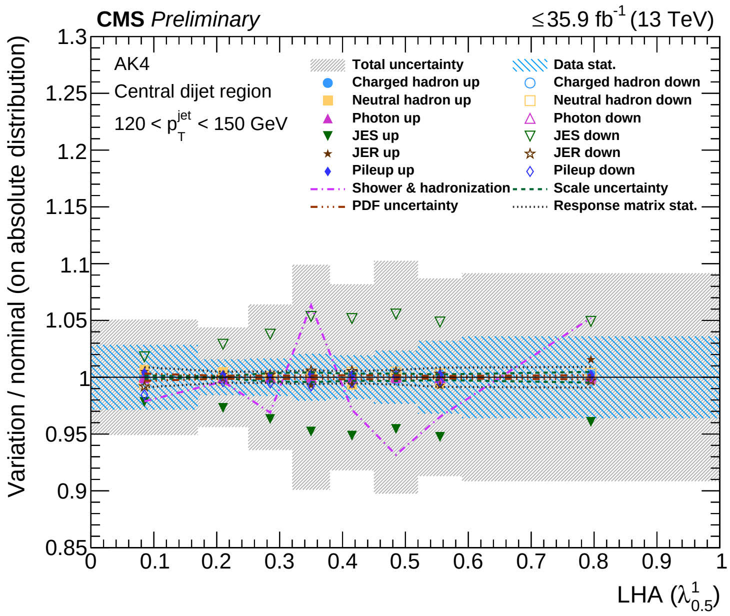

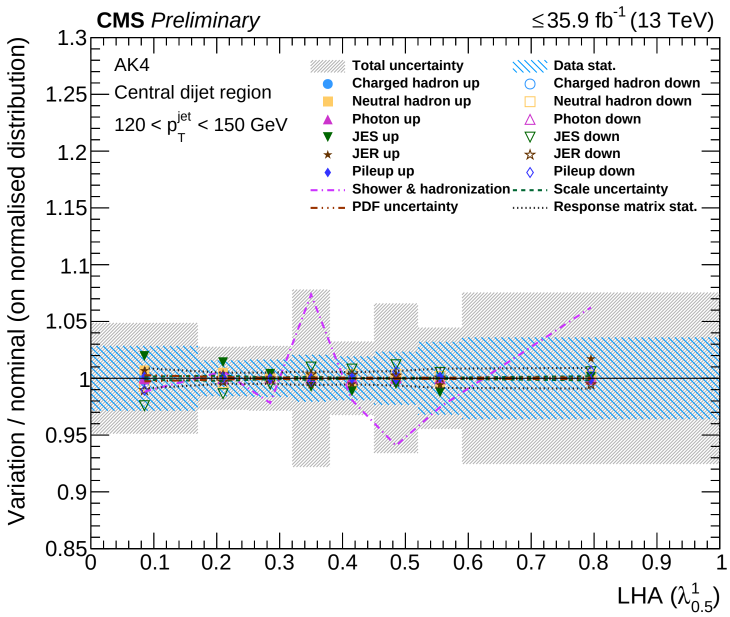

Figure 5: Ratio of the shifted distribution to the nominal distribution of ungroomed LHA ($\lambda^{1}_{0.5}$) for AK4 jets with $120 < p_{\mathrm{T}} < 150\,\mathrm{GeV}$ in the central dijet region before (left) and after (right) normalization. The darker hashed region indicates the statistical uncertainty of the experimental data, whilst the lighter hashed region represents the total uncertainty. The total uncertainty represents the sum in quadrature of statistical and systematic uncertainties. The single-sided uncertainty for shower and hadronization is estimated from HERWIG++ and is symmetrized for display in the total systematic uncertainty.

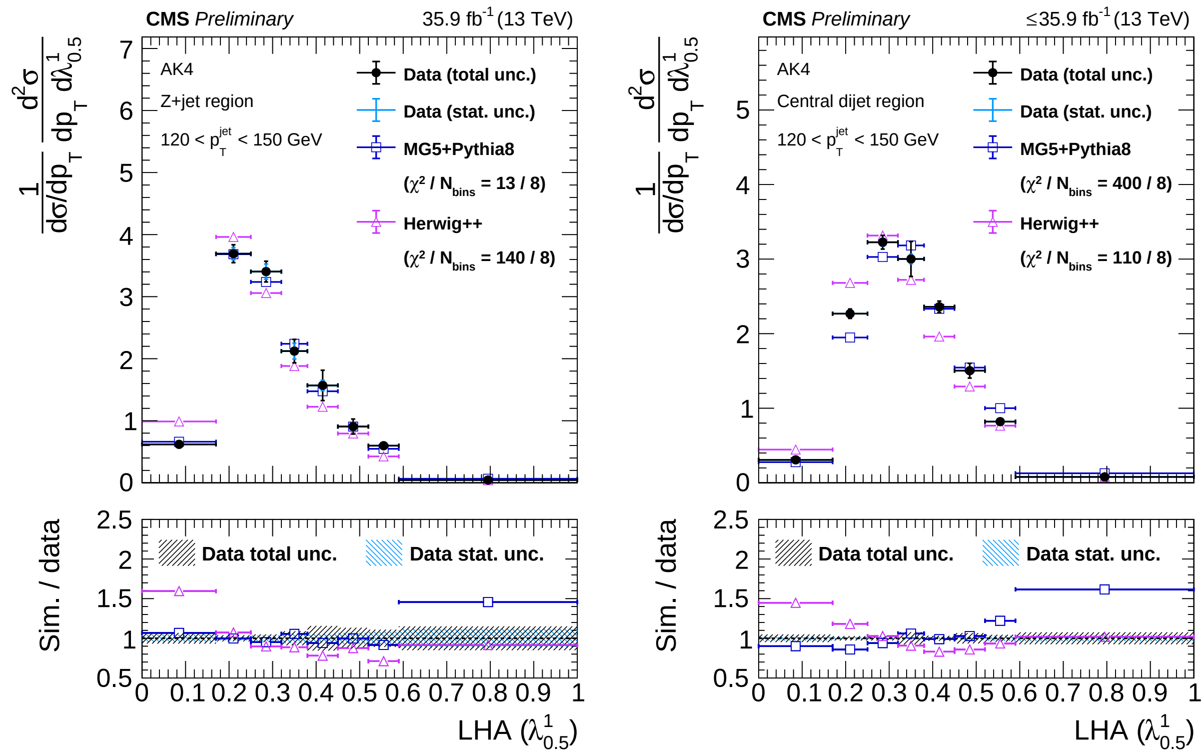

Figure 6: Particle-level distributions of ungroomed LHA ($\lambda^{1}_{0.5}$) in $120 < p_{\mathrm{T}} < 150$ GeV in the Z+jet region (left) and central dijet region (right). The light blue and black error bars correspond to the statistical and total uncertainties of the experimental data, respectively.

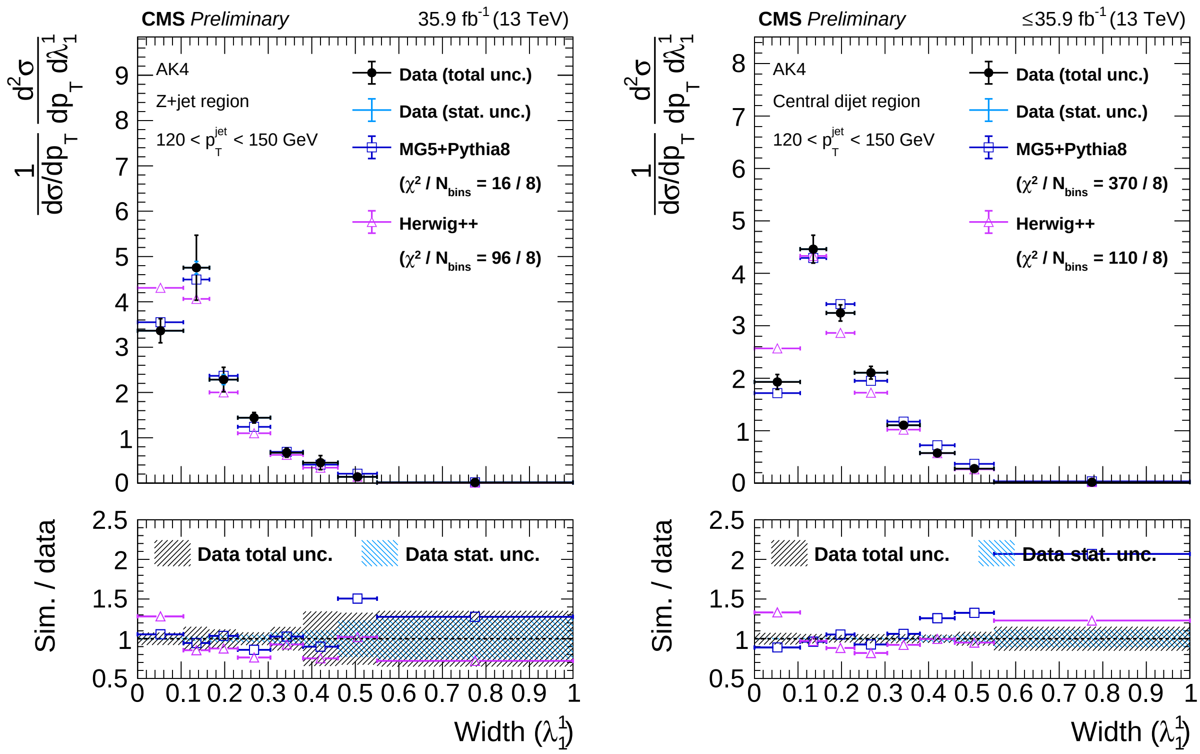

Figure 7: Particle-level distributions of ungroomed width (λ_1^1) in $120 < p_{\mathrm{T}} < 150$ GeV in the Z+jet region (left) and central dijet region (right). The light blue and black error bars correspond to the statistical and total uncertainties of the experimental data, respectively.

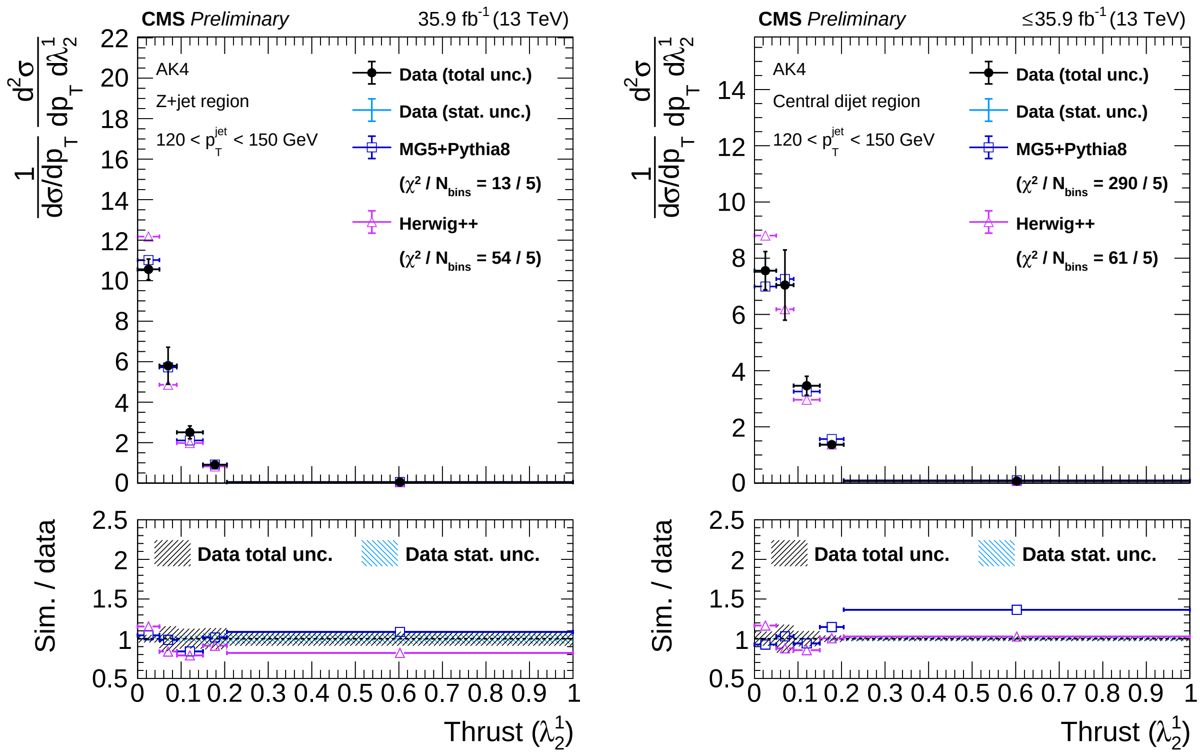

Figure 8: Particle-level distributions of ungroomed thrust (λ_2^1) in $120 < p_{\mathrm{T}} < 150$ GeV in the Z+jet region (left) and central dijet region (right). The light blue and black error bars correspond to the statistical and total uncertainties of the experimental data, respectively.

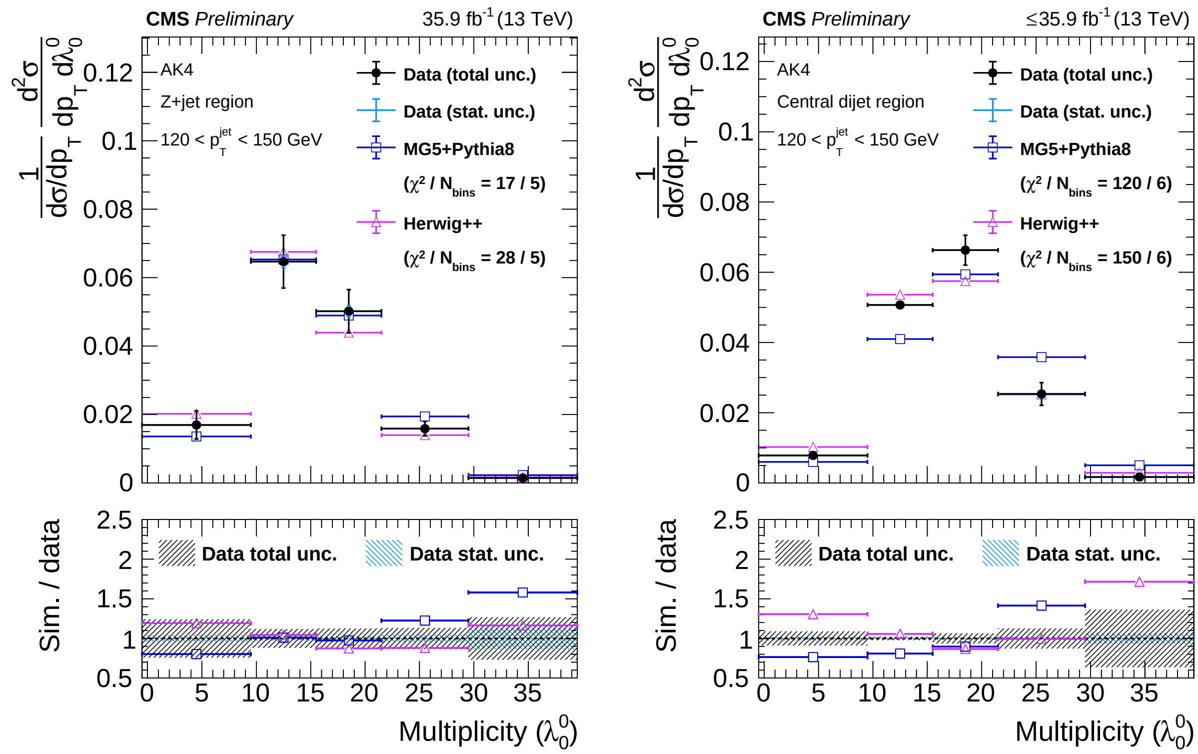

Figure 9: Particle-level distributions of ungroomed multiplicity (λ_0^0) in $120 < p_T < 150$ GeV in the Z+jet region (left) and central dijet region (right). The light blue and black error bars correspond to the statistical and total uncertainties of the experimental data, respectively.

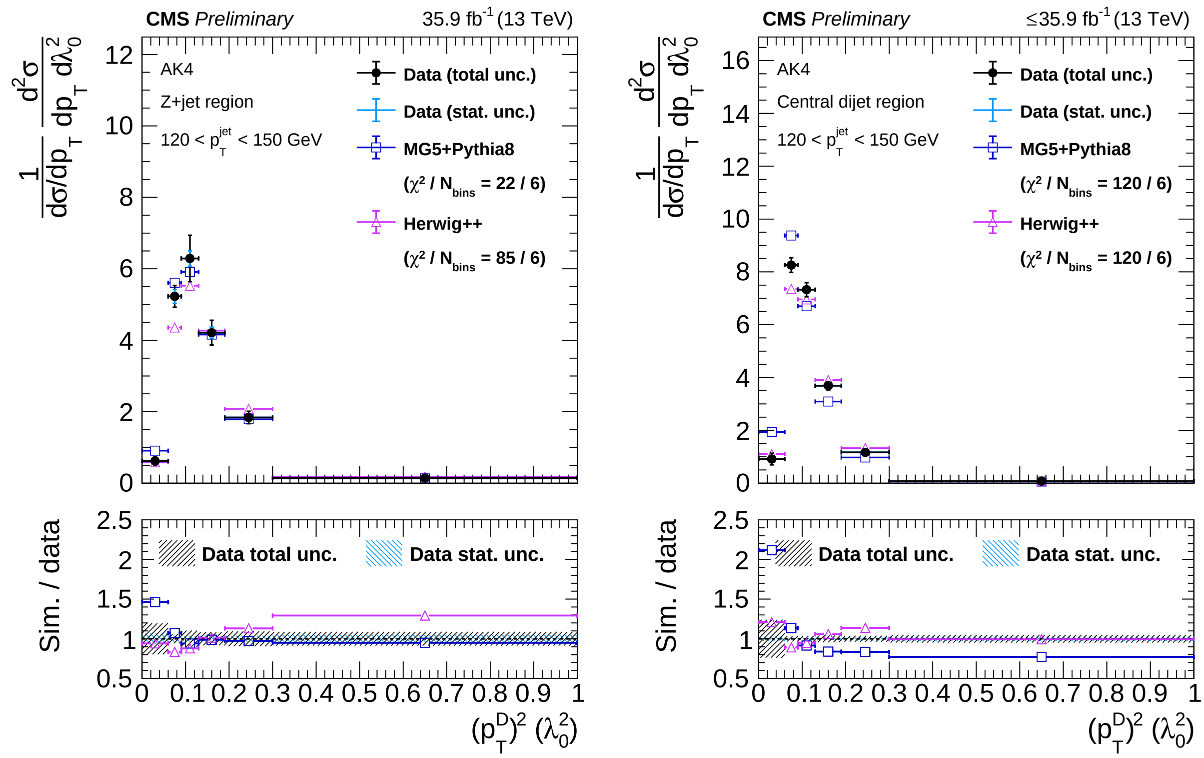

Figure 10: Particle-level distributions of ungroomed $(p_{\mathrm{T}}^{D})^2$ (λ_0^2) in $120 < p_{\mathrm{T}} < 150$ GeV in the Z+jet region (left) and central dijet region (right). The light blue and black error bars correspond to the statistical and total uncertainties of the experimental data, respectively.

Figure 11 shows multiple variants of LHA in the central dijet region. The level of data-to-simulation agreement of the generators for ungroomed AK4 jets with $1000 < p_{\mathrm{T}} < 4000\,\mathrm{GeV}$ (enriched in quark jets) is better in the low p_{T} central dijet region (enriched in gluon jets, Fig. 6, right), but worse than in the low p_{T} Z+jet region (Fig. 6, left). This is consistent with the hypothesis that the level of agreement is related to the expected gluon fraction in the sample. The LHA distribution for ungroomed AK8 jets with $120 < p_{\mathrm{T}} < 150\,\mathrm{GeV}$ and its level of agreement between data and simulation is similar to AK4 jets. The charged-only LHA distribution for ungroomed AK4 jets with $120 < p_{\mathrm{T}} < 150\,\mathrm{GeV}$ is wider than for LHA with charged+neutral constituents. The data-to-simulation agreement is similar in magnitude, suggesting that the majority of the underlying difference to experimental data in the simulation model may be probed using a charged-only observable. The LHA distribution for groomed AK4 jets with $120 < p_{\mathrm{T}} < 150\,\mathrm{GeV}$ is wider than for ungroomed jets. The data-to-simulation agreement for LHA in groomed jets is slightly better for both generators compared to that in ungroomed jets, which is expected since grooming suppresses effects from pileup, underlying event, and initial-state radiation, which are more difficult to model.

To study the behaviour of the measured jet substructure observables in the dimensions summarised in Table 3, we focus on the mean of each substructure distribution. In Fig. 12, the measured mean of ungroomed LHA ($\lambda^{1}_{0.5}$) for AK4 jets is shown as a function of jet p_{T}, including also predictions from more recent generators. The mean decreases as a function of the jet p_{T} in both the Z+jet and central dijet regions, as a result of constituents being located closer to the jet axis due to the larger Lorentz boost at higher p_{T}. This trend is displayed by all generators. The mean in the Z+jet region is well-described at low p_{T} and overestimated at high p_{T} by MG5+PYTHIA8, while all other generators significantly underestimate it across the whole p_{T} range. In the central dijet sample, MG5+PYTHIA8 and HERWIG++ generator predictions deviate significantly from the measurement. While MG5+PYTHIA8 predicts a larger mean than that measured in the experimental data, HERWIG++ underestimates it across the whole p_{T} range. HERWIG7 CH3 and PYTHIA8 CP2 provide the best description, followed by PYTHIA8 CP5 and SHERPA. One can infer from this observation that the data-to-simulation agreement depends on how generators model the difference between quark and gluon jets, consistent with previous measurements of observables related to jet fragmentation [23].

In Fig. 13, the behaviour of jet substructure observables across all dimensions under study is summarised using the mean of each distribution. The upper plot in Fig. 13 shows the results from CMS data and the MG5+PYTHIA8 and HERWIG++ simulations. Across most observables and dimensions, the measurements are found to be enveloped by the two generator predictions. The behaviour as a function of p_{T} and jet size, discussed previously for LHA, holds also for the other substructure observables.

The charged-only observables consistently show a similar data-to-simulation agreement compared to the charged+neutral observables. They are able to be measured with finer binning (e.g. comparing LHA in Fig. 11 (lower left) with Fig. 6 (right)), though their prediction involves more non-perturbative effects in the fragmentation than the charged+neutral observables. Each also has a smaller uncertainty relative to its respective charged+neutral observable. Both measurements are thus complementary and are found to give similar conclusions in terms of data-to-simulation agreement.

Finally, the groomed observables consistently show similar data-to-simulation agreement compared to their respective ungroomed observables. The same conclusion holds for the level of agreement between the two simulation predictions for groomed and ungroomed observables, consistent with what was concluded in Ref. [12]. Since the groomed observables may be com-

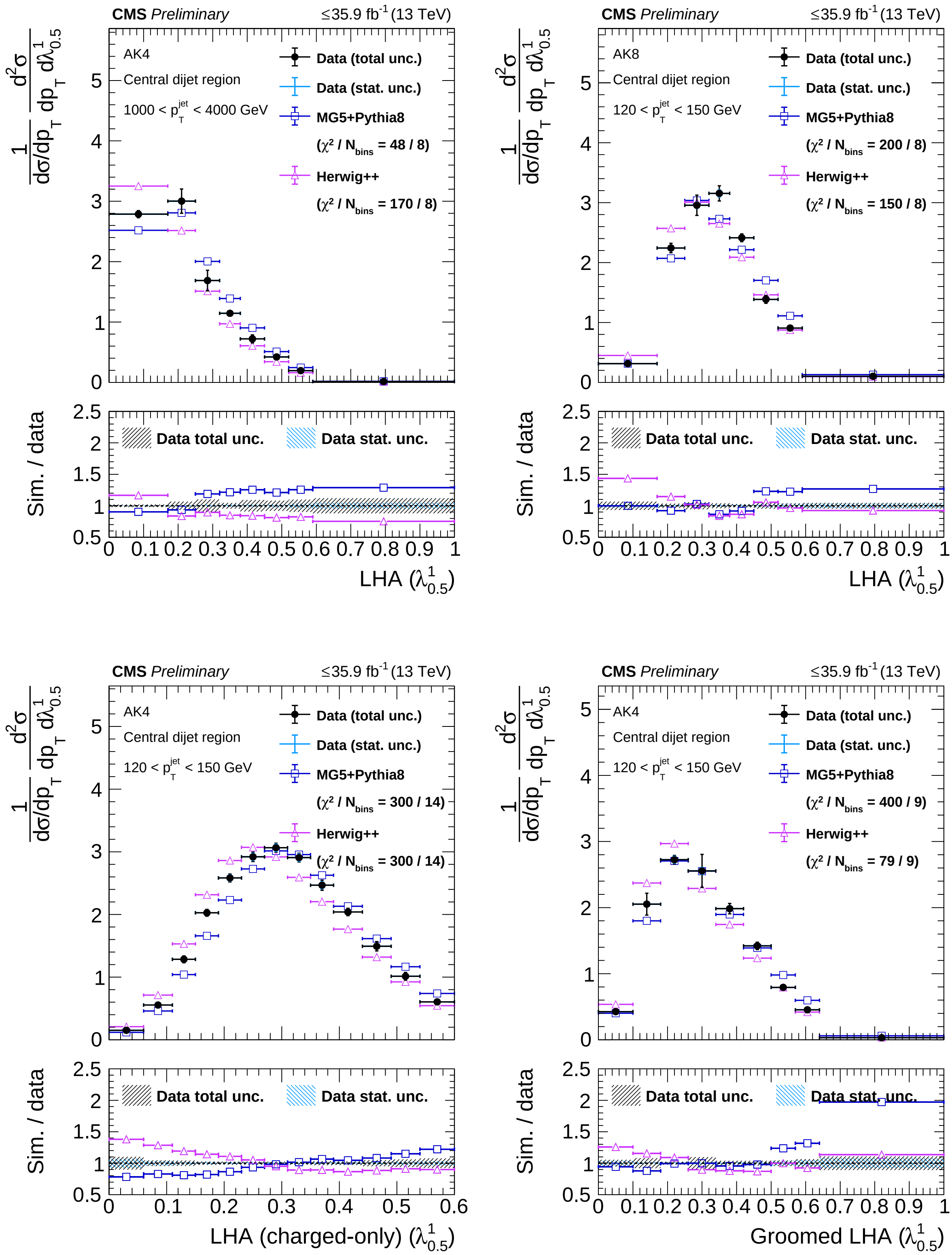

Figure 11: Particle-level distributions of variants of LHA ($\lambda^1_{0.5}$) in the central dijet region: (upper left) ungroomed AK4 $1000 < p_T < 4000$ GeV, (upper right) ungroomed AK8 $120 < p_T < 150$ GeV, (lower left) ungroomed charged-only AK4 $120 < p_T < 150$ GeV, (lower right) groomed AK4 $120 < p_T < 150$ GeV. The light blue and black error bars correspond to the statistical and total uncertainties of the experimental data, respectively.

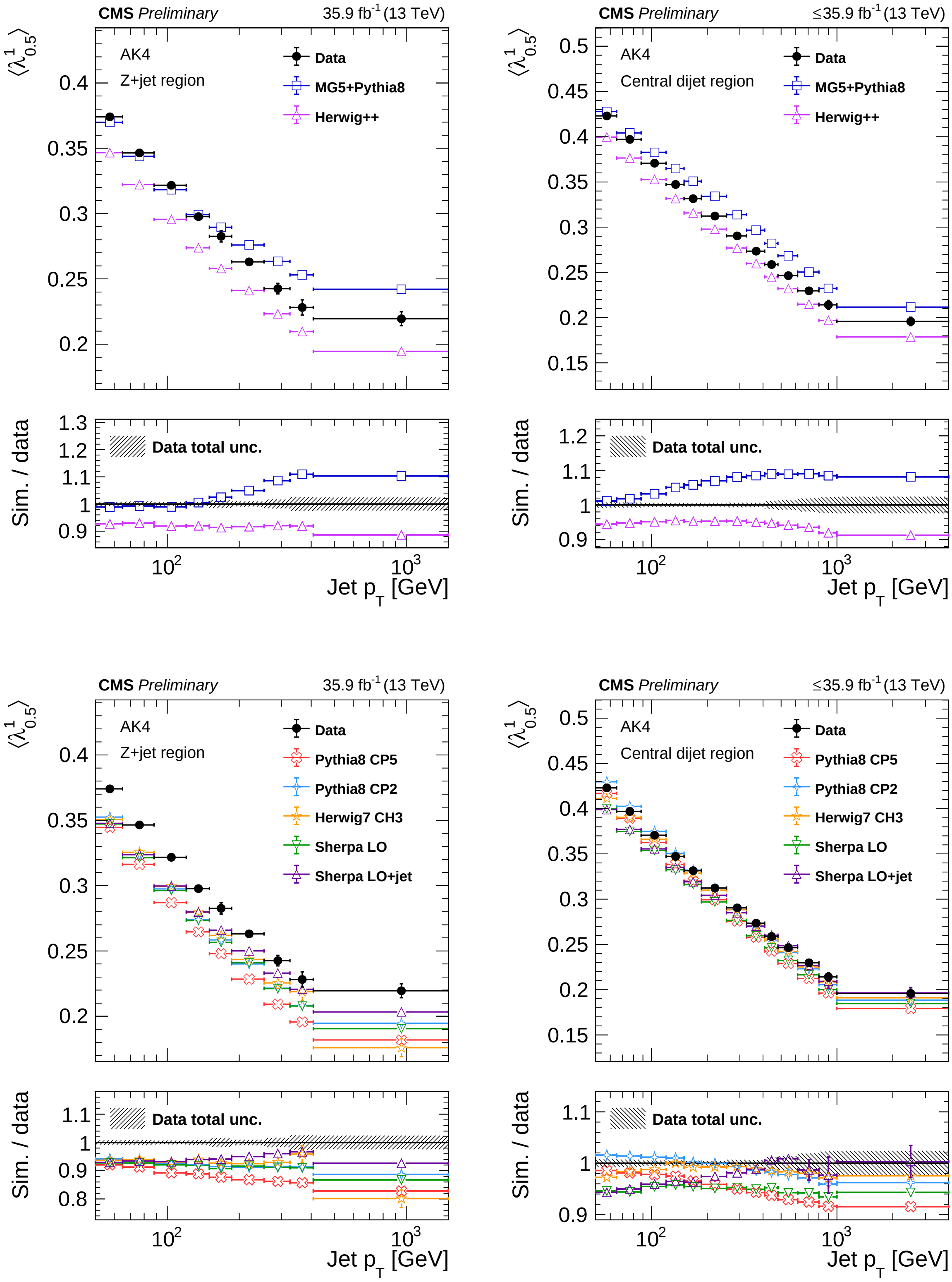

Figure 12: Mean of ungroomed LHA ($\lambda^{1}_{0.5}$) for AK4 jets as a function of p_{T} in the Z+jet (left) and central dijet region (right) regions. The error bars on the data and the hashed region in the ratio plot correspond to the total uncertainties of the experimental data. The error bars on the simulation correspond to the statistical uncertainties of the simulation.

puted with smaller theoretical uncertainties arising from non-perturbative effects, they allow for better study of the prediction of perturbative emissions. From the measured data, one may infer that the differences between the simulation models in terms of modelling perturbative emissions capture the effects that lead to the data-to-simulation disagreements.

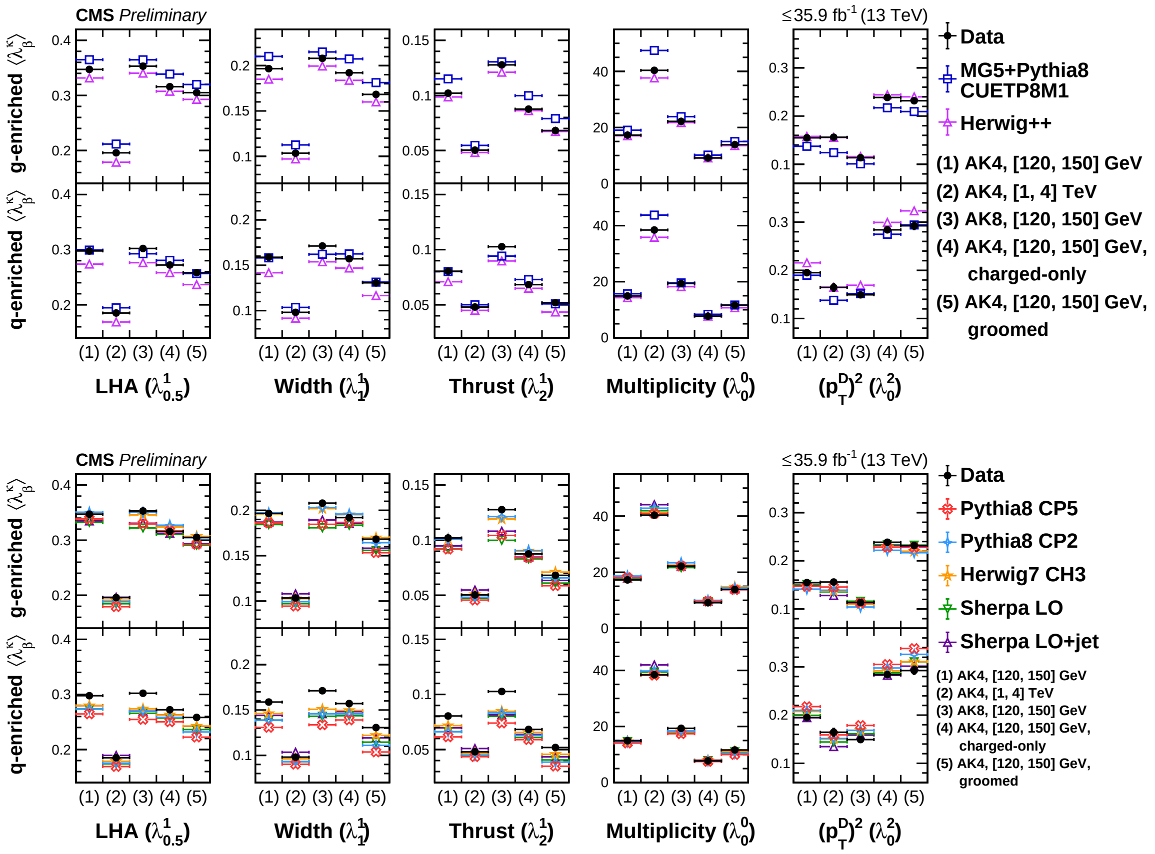

Figure 13: Mean of substructure observables in regions with gluon-enriched and quark-enriched jets, for the following configurations: (1) ungroomed AK4 $120 < p_{\mathrm{T}} < 150\,\mathrm{GeV}$, (2) ungroomed AK4 $1000 < p_{\mathrm{T}} < 4000\,\mathrm{GeV}$, (3) ungroomed AK8 $120 < p_{\mathrm{T}} < 150\,\mathrm{GeV}$, (4) ungroomed charged-only AK4 $120 < p_{\mathrm{T}} < 150\,\mathrm{GeV}$, and (5) groomed AK4 $120 < p_{\mathrm{T}} < 150\,\mathrm{GeV}$; shown for each of the observables LHA ($\lambda^1_{0.5}$), width (λ^1_1), thrust (λ^1_2), multiplicity (λ^0_0), and $(p_{\mathrm{T}}^D)^2$ (λ^2_0). The central jet in the dijet region is used for the gluon-enriched sample, whilst for the quark-enriched sample the jet in the Z+jet region is used for $120 < p_{\mathrm{T}} < 150\,\mathrm{GeV}$, and the forward jet in the dijet region is used for $1000 < p_{\mathrm{T}} < 4000\,\mathrm{GeV}$. The error bars on the data correspond to the total uncertainties of the experimental data. The error bars on the simulation correspond to the statistical uncertainties of the simulation.

In Fig. 13 (lower), the same measured data are compared to predictions from more recent generators. In the gluon-enriched sample, HERWIG7 CH3, PYTHIA8 CP5, PYTHIA8 CP2, and SHERPA generally provide a better description than either HERWIG++ or MG5+PYTHIA8. In the quark-enriched sample, MG5+PYTHIA8 provides the best description, followed by HERWIG7, PYTHIA8 CP2, SHERPA, HERWIG++, and PYTHIA8 CP5. Thus, the previous observations in Fig. 13 (upper) of more accurate modelling of quark jet substructure, and less accurate modelling of gluon jet substructure, does not necessarily hold for more recent generators and tunes under study. Improved modelling of gluon jets at the cost of poorer modelling of quark jets is observed. Besides the more recent generator versions and tunes used for HERWIG and PYTHIA8, an important difference among the predictions is the choice of $\alpha_S(m_Z)$ in the final state shower, to which the jet substructure modelling is sensitive [39]. The PYTHIA8 CP2 prediction using $\alpha_S(m_Z) = 0.130$ predicts systematically larger values of LHA, width, thrust, and multiplicity, and smaller value of $(p_T^D)^2$, for both quarks and gluons than the PYTHIA8 CP5 prediction using $\alpha_S(m_Z) = 0.118$.

In Fig. 14, the ratio of the means in the gluon-enriched and quark-enriched samples is shown, illustrating how well the generators model both the differences between quarks and gluons, and the relative quark/gluon composition of the samples. As previously mentioned, gluon jets exhibit, on average, larger values of LHA, width, thrust, and multiplicity, and smaller values of $(p_T^D)^2$, than quark jets. At low p_T, the ratio of the means in the central dijet and Z+jet regions is found to be significantly larger than unity for LHA, width, thrust, and multiplicity, and significantly smaller for $(p_T^D)^2$, indicating that these observables have significant separation power between quark and gluon jets. Strikingly, all generators overestimate the difference between quark and gluon jets at low p_T when compared to experimental data. At high p_T however, the ratio of the means in the central and forward dijet regions is significantly closer to unity, and all generators give a reasonable description of the ratio that is consistent with that measured in data. The gluon- and quark-enriched samples are each expected to have a more equal relative quark/gluon jet composition at this p_T (see Fig. 1). The best overall data-to-simulation agreement for the ratio is achieved by SHERPA, followed by HERWIG++, MG5+PYTHIA8, HERWIG7 CH3, PYTHIA8 CP2, and PYTHIA8 CP5. The PYTHIA8 CP2 and CP5 predictions are very similar, showing that the quark and gluon discrimination power is not governed by the choice of $\alpha_S(m_Z)$ in the final state shower, but rather by the model used for jet fragmentation. Comparing the behaviour of SHERPA LO to LO+jet, the effect of the additional outgoing partons is an improvement in the description of the ratio of the means in the gluon-enriched and quark-enriched samples. Since the additional outgoing partons can affect the fraction of gluon jets in the signal regions, this demonstrates that the measurement of the ratio provides information not only about the differences between quarks and gluons, but also about the fraction of gluon jets.

8 Summary

Measurements of distributions of generalized jet angularities in pp collision data taken at $\sqrt{s} = 13$ TeV in dijet and for the first time also in Z+jet topologies have been presented. While the dijet topology allows access to a sample of jets that predominantly originate from gluon fragmentation, the Z+jet topology yields a sample enriched in quark-initiated jets. A set of five generalized angularities is measured to study different features in the modelling of jet substructure observables. Three infrared and collinear-safe angularities are particularly sensitive to the modelling of perturbative emissions in jets, while the other two have larger contributions from non-perturbative effects. For the first time, a study of angularities with different jet radii, both with and without the application of a grooming algorithm, was carried out to further discriminate between different features in the modelling. It was found that the measurements for quark and gluon jets yield values in between the predictions from the MG5+PYTHIA8 and HERWIG++ simulations. The quality of modelling for the infrared and collinear-safe angularities is found to be sensitive to the quark and gluon composition of the sample of jets. It is also found to be largely independent of whether a grooming algorithm is applied, suggesting that the quality depends mainly on the perturbative emissions in jets, rather than non-perturbative effects. A comparison of the means of the angularities in quark- and gluon-enriched data samples demonstrated their discrimination power, which was found to be overestimated by all generators under study, showing the clear need for improvements in the MC. In outlook, this measurement will allow a detailed analysis of the assumptions and approximations made in calculations and Monte Carlo simulations of jet substructure, ideally yielding better predictions

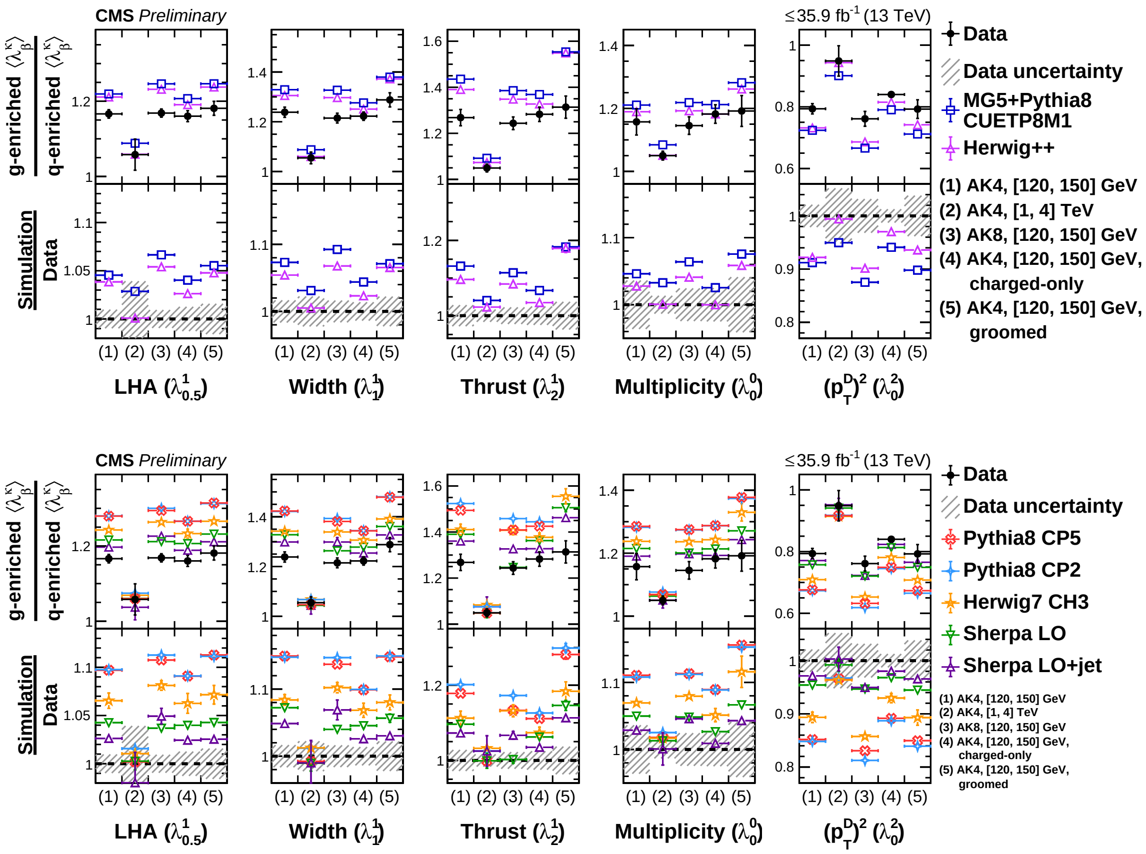

Figure 14: Ratio of the mean of substructure observables in regions with gluon-enriched and quark-enriched jets, for the following configurations: (1) ungroomed AK4 $120 < p_{\mathrm{T}} < 150\,\mathrm{GeV}$, (2) ungroomed AK4 $1000 < p_{\mathrm{T}} < 4000\,\mathrm{GeV}$, (3) ungroomed AK8 $120 < p_{\mathrm{T}} < 150\,\mathrm{GeV}$, (4) ungroomed charged-only AK4 $120 < p_{\mathrm{T}} < 150\,\mathrm{GeV}$, and (5) groomed AK4 $120 < p_{\mathrm{T}} < 150\,\mathrm{GeV}$; for the observables LHA ($\lambda^{1}_{0.5}$), width (λ^{1}_{1}), thrust (λ^{1}_{2}), multiplicity (λ^{0}_{0}), and $(p_{\mathrm{T}}^{D})^{2}$ (λ^{2}_{0}). The central jet in the dijet region is used for the gluon-enriched sample, whilst for the quark-enriched sample the jet in the Z+jet region is used for $120 < p_{\mathrm{T}} < 150\,\mathrm{GeV}$, and the forward jet in the dijet region is used for $1000 < p_{\mathrm{T}} < 4000\,\mathrm{GeV}$. The error bars on the data correspond to the total uncertainties of the experimental data. The error bars on the simulation correspond to the statistical uncertainties of the simulation.

for experimental searches and measurements that rely on jet substructure.

References

[1] G. P. Salam, "Towards jetography", *Eur. Phys. J. C* **67** (2010) 637, doi:10.1140/epjc/s10052-010-1314-6, arXiv:0906.1833.

[2] R. Kogler et al., "Jet substructure at the Large Hadron Collider: experimental review", *Rev. Mod. Phys.* **91** (2019) 045003, doi:10.1103/RevModPhys.91.045003, arXiv:1803.06991.

[3] A. J. Larkoski, I. Moult, and B. Nachman, "Jet substructure at the Large Hadron Collider: a review of recent advances in theory and Machine Learning", *Phys. Rept.* **841** (2020) 1, doi:10.1016/j.physrep.2019.11.001, arXiv:1709.04464.

[4] S. Marzani, G. Soyez, and M. Spannowsky, "Looking inside jets: an introduction to jet substructure and boosted-object phenomenology", volume 958. Springer, 2019. doi:10.1007/978-3-030-15709-8.

[5] K. Konishi, A. Ukawa, and G. Veneziano, "Jet calculus: a simple algorithm for resolving QCD jets", *Nuclear Physics B* **157** (1979) 45, doi:10.1016/0550-3213(79)90053-1.

[6] OPAL Collaboration, "A study of differences between quark and gluon jets using vertex tagging of quark jets", *Zeitschrift für Physik C Particles and Fields* **58** (1993) 387, doi:10.1007/BF01557696.

[7] OPAL Collaboration, "A model independent measurement of quark and gluon jet properties and differences", *Zeitschrift für Physik C Particles and Fields* **68** (1995) 179, doi:10.1007/BF01566667.

[8] DELPHI Collaboration, "Energy dependence of the differences between the quark and gluon jet fragmentation", *Zeitschrift für Physik C Particles and Fields* **70** (1996) 179, doi:10.1007/s002880050095.

[9] ALEPH Collaboration, "Measurements of the structure of quark and gluon jets in hadronic Z decays", *Eur. Phys. J. C* **17** (2000) 1, doi:epjc/v17/p1(epjc0474).

[10] ALEPH Collaboration, "Quark and gluon jet properties in symmetric three-jet events", *Physics Letters B* **384** (1996) 353, doi:https://doi.org/10.1016/0370-2693(96)00849-0.

[11] ALEPH Collaboration, "Studies of quantum chromodynamics with the ALEPH detector", *Phys. Rept.* **294** (1998) 1, doi:10.1016/S0370-1573(97)00045-8.

[12] P. Gras et al., "Systematics of quark/gluon tagging", *JHEP* **07** (2017) 091, doi:10.1007/JHEP07(2017)091, arXiv:1704.03878.

[13] ATLAS Collaboration, "Properties of jet fragmentation using charged particles measured with the ATLAS detector in pp collisions at $\sqrt{s} = 13$ TeV", *Phys. Rev. D* **100** (2019) 052011, doi:10.1103/PhysRevD.100.052011, arXiv:1906.09254.

[14] ATLAS Collaboration, "Properties of $g \to b\bar{b}$ at small opening angles in pp collisions with the ATLAS detector at $\sqrt{s} = 13$ TeV", *Phys. Rev. D* **99** (2019) 052004, doi:10.1103/PhysRevD.99.052004, arXiv:1812.09283.

[15] ATLAS Collaboration, "Measurement of jet fragmentation in 5.02 TeV proton-lead and proton-proton collisions with the ATLAS detector", *Nucl. Phys. A* **978** (2018) 65, doi:10.1016/j.nuclphysa.2018.07.006, arXiv:1706.02859.

[16] ATLAS Collaboration, "Measurement of jet fragmentation in Pb+Pb and pp collisions at $\sqrt{s_{\mathrm{NN}}} = 2.76$ TeV with the ATLAS detector at the LHC", *Eur. Phys. J. C* **77** (2017) 379, doi:10.1140/epjc/s10052-017-4915-5, arXiv:1702.00674.

[17] ATLAS Collaboration, "Measurement of the charged-particle multiplicity inside jets from $\sqrt{s} = 8$ TeV pp collisions with the ATLAS detector", *Eur. Phys. J. C* **76** (2016) 322, doi:10.1140/epjc/s10052-016-4126-5, arXiv:1602.00988.

[18] ATLAS Collaboration, "Measurement of the jet fragmentation function and transverse profile in proton-proton collisions at a center-of-mass energy of 7 TeV with the ATLAS detector", *Eur. Phys. J. C* **71** (2011) 1795, doi:10.1140/epjc/s10052-011-1795-y, arXiv:1109.5816.

[19] ATLAS Collaboration, "Properties of jets measured from tracks in proton-proton collisions at center-of-mass energy $\sqrt{s} = 7$ TeV with the ATLAS detector", *Phys. Rev. D* **84** (2011) 054001, doi:10.1103/PhysRevD.84.054001, arXiv:1107.3311.

[20] CMS Collaboration, "Jet shapes of isolated photon-tagged jets in Pb-Pb and pp collisions at $\sqrt{s_{\mathrm{NN}}} = 5.02$ TeV", *Phys. Rev. Lett.* **122** (2019) 152001, doi:10.1103/PhysRevLett.122.152001, arXiv:1809.08602.

[21] CMS Collaboration, "Measurement of the splitting function in pp and Pb-Pb collisions at $\sqrt{s_{_{\mathrm{NN}}}} = 5.02$ TeV", *Phys. Rev. Lett.* **120** (2018) 142302, doi:10.1103/PhysRevLett.120.142302, arXiv:1708.09429.

[22] CMS Collaboration, "Measurement of jet fragmentation in PbPb and pp collisions at $\sqrt{s_{NN}} = 2.76$ TeV", *Phys. Rev. C* **90** (2014) 024908, doi:10.1103/PhysRevC.90.024908, arXiv:1406.0932.

[23] CMS Collaboration, "Shape, transverse size, and charged hadron multiplicity of jets in pp collisions at 7 TeV", *JHEP* **06** (2012) 160, doi:10.1007/JHEP06(2012)160, arXiv:1204.3170.

[24] CMS Collaboration, "Measurement of jet fragmentation into charged particles in pp and PbPb collisions at $\sqrt{s_{NN}} = 2.76$ TeV", *JHEP* **10** (2012) 087, doi:10.1007/JHEP10(2012)087, arXiv:1205.5872.

[25] ALICE Collaboration, "Jet fragmentation transverse momentum measurements from di-hadron correlations in $\sqrt{s}$ = 7 TeV pp and $\sqrt{s_{\mathrm{NN}}}$ = 5.02 TeV p-Pb collisions", *JHEP* **03** (2019) 169, doi:10.1007/JHEP03(2019)169, arXiv:1811.09742.

[26] ALICE Collaboration, "Charged jet cross section and fragmentation in proton-proton collisions at $\sqrt{s}$ = 7 TeV", *Phys. Rev. D* **99** (2019) 012016, doi:10.1103/PhysRevD.99.012016, arXiv:1809.03232.

[27] LHCb Collaboration, "Measurement of charged hadron production in Z-tagged jets in proton-proton collisions at $\sqrt{s} = 8$ TeV", *Phys. Rev. Lett.* **123** (2019) 232001, doi:10.1103/PhysRevLett.123.232001, arXiv:1904.08878.

[28] ATLAS Collaboration, "Measurement of the Lund jet plane using charged particles in 13 TeV proton-proton collisions with the ATLAS detector", *Phys. Rev. Lett.* **124** (2020) 222002, doi:10.1103/PhysRevLett.124.222002, arXiv:2004.03540.

[29] ATLAS Collaboration, "Measurement of soft-drop jet observables in pp collisions with the ATLAS detector at $\sqrt{s}$ =13 TeV", *Phys. Rev. D* **101** (2020) 052007, doi:10.1103/PhysRevD.101.052007, arXiv:1912.09837.

[30] ATLAS Collaboration, "Measurement of jet-substructure observables in top quark, W boson and light jet production in proton-proton collisions at $\sqrt{s} = 13$ TeV with the ATLAS detector", *JHEP* **08** (2019) 033, doi:10.1007/JHEP08(2019)033, arXiv:1903.02942.

[31] ATLAS Collaboration, "Measurement of the jet mass in high transverse momentum $Z(\to b\bar{b})\gamma$ production at $\sqrt{s} = 13$ TeV using the ATLAS detector", *Phys. Lett. B* **812** (2021) 135991, doi:10.1016/j.physletb.2020.135991, arXiv:1907.07093.

[32] ATLAS Collaboration, "Measurement of colour flow using jet-pull observables in $t\bar{t}$ events with the ATLAS experiment at $\sqrt{s} = 13$ TeV", *Eur. Phys. J. C* **78** (2018) 847, doi:10.1140/epjc/s10052-018-6290-2, arXiv:1805.02935.

[33] ATLAS Collaboration, "Measurement of the soft-drop jet mass in pp collisions at $\sqrt{s} = 13$ TeV with the ATLAS detector", *Phys. Rev. Lett.* **121** (2018) 092001, doi:10.1103/PhysRevLett.121.092001, arXiv:1711.08341.

[34] ATLAS Collaboration, "Measurement of colour flow with the jet pull angle in $t\bar{t}$ events using the ATLAS detector at $\sqrt{s} = 8$ TeV", *Phys. Lett. B* **750** (2015) 475, doi:10.1016/j.physletb.2015.09.051, arXiv:1506.05629.

[35] ATLAS Collaboration, "Measurement of jet charge in dijet events from $\sqrt{s}$=8 TeV pp collisions with the ATLAS detector", *Phys. Rev. D* **93** (2016) 052003, doi:10.1103/PhysRevD.93.052003, arXiv:1509.05190.

[36] ATLAS Collaboration, "Measurement of jet shapes in top-quark pair events at $\sqrt{s}$ = 7 TeV using the ATLAS detector", *Eur. Phys. J. C* **73** (2013) 2676, doi:10.1140/epjc/s10052-013-2676-3, arXiv:1307.5749.

[37] ATLAS Collaboration, "ATLAS measurements of the properties of jets for boosted particle searches", *Phys. Rev. D* **86** (2012) 072006, doi:10.1103/PhysRevD.86.072006, arXiv:1206.5369.

[38] ATLAS Collaboration, "Jet mass and substructure of inclusive jets in $\sqrt{s} = 7$ TeV pp collisions with the ATLAS experiment", *JHEP* **05** (2012) 128, doi:10.1007/JHEP05(2012)128, arXiv:1203.4606.

[39] CMS Collaboration, "Measurement of jet substructure observables in $\mathrm{t\bar{t}}$ events from proton-proton collisions at $\sqrt{s} = 13$ TeV", *Phys. Rev. D* **98** (2018) 092014, doi:10.1103/PhysRevD.98.092014, arXiv:1808.07340.

[40] CMS Collaboration, "Measurements of the differential jet cross section as a function of the jet mass in dijet events from proton-proton collisions at $\sqrt{s} = 13$ TeV", *JHEP* **11** (2018) 113, doi:10.1007/JHEP11(2018)113, arXiv:1807.05974.

[41] CMS Collaboration, "Measurement of the jet mass in highly boosted $\mathrm{t\bar{t}}$ events from pp collisions at $\sqrt{s} = 8$ TeV", *Eur. Phys. J. C* **77** (2017) 467, doi:10.1140/epjc/s10052-017-5030-3, arXiv:1703.06330.

[42] CMS Collaboration, "Measurements of jet charge with dijet events in pp collisions at $\sqrt{s} = 8$ TeV", *JHEP* **10** (2017) 131, doi:10.1007/JHEP10(2017)131, arXiv:1706.05868.

[43] CMS Collaboration, "Studies of jet mass in dijet and W/Z + jet events", *JHEP* **05** (2013) 090, doi:10.1007/JHEP05(2013)090, arXiv:1303.4811.

[44] A. J. Larkoski, J. Thaler, and W. J. Waalewijn, "Gaining (mutual) information about quark/gluon discrimination", *JHEP* **11** (2014) 129, doi:10.1007/JHEP11(2014)129, arXiv:1408.3122.

[45] CMS Collaboration, "Performance of quark/gluon discrimination in 8 TeV pp data", CMS Physics Analysis Summary CMS-PAS-JME-13-002, 2013.

[46] CMS Collaboration, "Jet algorithms performance in 13 TeV data", CMS Physics Analysis Summary CMS-PAS-JME-16-003, 2019.

[47] ATLAS Collaboration, "Light-quark and gluon jet discrimination in *pp* collisions at $\sqrt{s} = 7$ TeV with the ATLAS detector", *Eur. Phys. J. C* **74** (2014) 3023, doi:10.1140/epjc/s10052-014-3023-z, arXiv:1405.6583.

[48] A. J. Larkoski, S. Marzani, G. Soyez, and J. Thaler, "Soft drop", *JHEP* **05** (2014) 146, doi:10.1007/JHEP05(2014)146, arXiv:1402.2657.

[49] CMS Collaboration, "The CMS experiment at the CERN LHC", *JINST* **3** (2008) S08004, doi:10.1088/1748-0221/3/08/S08004.

[50] CMS Collaboration, "Particle-flow reconstruction and global event description with the CMS detector", *JINST* **12** (2017) P10003, doi:10.1088/1748-0221/12/10/P10003, arXiv:1706.04965.

[51] CMS Collaboration, "Description and performance of track and primary-vertex reconstruction with the CMS tracker", *JINST* **9** (2014) P10009, doi:10.1088/1748-0221/9/10/P10009, arXiv:1405.6569.

[52] M. Cacciari, G. P. Salam, and G. Soyez, "The anti-k_{T} jet clustering algorithm", *JHEP* **04** (2008) 063, doi:10.1088/1126-6708/2008/04/063, arXiv:0802.1189.

[53] M. Cacciari, G. P. Salam, and G. Soyez, "FastJet user manual", *Eur. Phys. J. C* **72** (2012) 1896, doi:10.1140/epjc/s10052-012-1896-2, arXiv:1111.6097.

[54] CMS Collaboration, "Performance of photon reconstruction and identification with the CMS detector in proton-proton collisions at $\sqrt{s} = 8$ TeV", *JINST* **10** (2015) P08010, doi:10.1088/1748-0221/10/08/P08010, arXiv:1502.02702.

[55] CMS Collaboration, "Pileup mitigation at CMS in 13 TeV data", *JINST* **15** (2020) P09018, doi:10.1088/1748-0221/15/09/p09018, arXiv:2003.00503.

[56] D. Bertolini, P. Harris, M. Low, and N. Tran, "Pileup per particle identification", *JHEP* **10** (2014) 059, doi:10.1007/JHEP10(2014)059, arXiv:1407.6013.

[57] CMS Collaboration, "Jet energy scale and resolution in the CMS experiment in pp collisions at 8 TeV", *JINST* **12** (2017) P02014, doi:10.1088/1748-0221/12/02/P02014, arXiv:1607.03663.

[58] CMS Collaboration, "The CMS trigger system", *JINST* **12** (2017) P01020, doi:10.1088/1748-0221/12/01/P01020, arXiv:1609.02366.

[59] CMS Collaboration, "Performance of the CMS muon trigger system in proton-proton collisions at $\sqrt{s} = 13$ TeV", (2021). arXiv:2102.04790. Submitted to *JINST*.

[60] J. Alwall et al., "The automated computation of tree-level and next-to-leading order differential cross sections, and their matching to parton shower simulations", *JHEP* **07** (2014) 079, doi:10.1007/JHEP07(2014)079, arXiv:1405.0301.

[61] T. Sjöstrand et al., "An introduction to PYTHIA 8.2", *Comput. Phys. Commun.* **191** (2015) 159, doi:10.1016/j.cpc.2015.01.024, arXiv:1410.3012.

[62] B. Andersson, G. Gustafson, G. Ingelman, and T. Sjöstrand, "Parton fragmentation and string dynamics", *Phys. Rept.* **97** (1983) 31, doi:10.1016/0370-1573(83)90080-7.

[63] T. Sjöstrand, "The merging of jets", *Phys. Lett. B* **142** (1984) 420, doi:10.1016/0370-2693(84)91354-6.

[64] J. Alwall et al., "Comparative study of various algorithms for the merging of parton showers and matrix elements in hadronic collisions", *Eur. Phys. J. C* **53** (2008) 473, doi:10.1140/epjc/s10052-007-0490-5, arXiv:0706.2569.

[65] P. Skands, S. Carrazza, and J. Rojo, "Tuning PYTHIA 8.1: the Monash 2013 tune", *Eur. Phys. J. C* **74** (2014) 3024, doi:10.1140/epjc/s10052-014-3024-y, arXiv:1404.5630.

[66] CMS Collaboration, "Event generator tunes obtained from underlying event and multiparton scattering measurements", *Eur. Phys. J. C* **76** (2016) 155, doi:10.1140/epjc/s10052-016-3988-x, arXiv:1512.00815.

[67] M. Bahr et al., "Herwig++ physics and manual", *Eur. Phys. J. C* **58** (2008) 639, doi:10.1140/epjc/s10052-008-0798-9, arXiv:0803.0883.

[68] J. Bellm et al., "Herwig++ 2.7 release note", arXiv:1310.6877.

[69] M. H. Seymour and A. Siodmok, "Constraining MPI models using σ_{eff} and recent Tevatron and LHC underlying event data", *JHEP* **10** (2013) 113, doi:10.1007/JHEP10(2013)113, arXiv:1307.5015.

[70] J. M. Lindert et al., "Precise predictions for $V+$ jets dark matter backgrounds", *Eur. Phys. J. C* **77** (2017) 829, doi:10.1140/epjc/s10052-017-5389-1, arXiv:1705.04664.

[71] NNPDF Collaboration, "Parton distributions for the LHC Run II", *JHEP* **04** (2015) 040, doi:10.1007/JHEP04(2015)040, arXiv:1410.8849.

[72] GEANT4 Collaboration, "GEANT4—a simulation toolkit", *Nucl. Instrum. Meth. A* **506** (2003) 250, doi:10.1016/S0168-9002(03)01368-8.

[73] CMS Collaboration, "Extraction and validation of a new set of CMS PYTHIA8 tunes from underlying-event measurements", *Eur. Phys. J. C* **80** (2020) 4, doi:10.1140/epjc/s10052-019-7499-4, arXiv:1903.12179.

[74] J. Bellm et al., "Herwig 7.0/Herwig++ 3.0 release note", *Eur. Phys. J. C* **76** (2016) 196, doi:10.1140/epjc/s10052-016-4018-8, arXiv:1512.01178.

[75] CMS Collaboration, "Development and validation of HERWIG 7 tunes from CMS underlying-event measurements", (2020). arXiv:2011.03422. Submitted to *Eur. Phys. J. C*.

[76] Sherpa Collaboration, "Event generation with Sherpa 2.2", *SciPost Phys.* **7** (2019) 034, doi:10.21468/SciPostPhys.7.3.034, arXiv:1905.09127.

[77] F. Krauss, R. Kuhn, and G. Soff, "AMEGIC++ 1.0: a matrix element generator in C++", *JHEP* **02** (2002) 044, doi:10.1088/1126-6708/2002/02/044, arXiv:hep-ph/0109036.

[78] T. Gleisberg and S. Hoeche, "Comix, a new matrix element generator", *JHEP* **12** (2008) 039, doi:10.1088/1126-6708/2008/12/039, arXiv:0808.3674.

[79] S. Catani, F. Krauss, R. Kuhn, and B. R. Webber, "QCD matrix elements + parton showers", *JHEP* **11** (2001) 063, doi:10.1088/1126-6708/2001/11/063, arXiv:hep-ph/0109231.

[80] F. Krauss, "Matrix elements and parton showers in hadronic interactions", *JHEP* **08** (2002) 015, doi:10.1088/1126-6708/2002/08/015, arXiv:hep-ph/0205283.

[81] A. Schalicke and F. Krauss, "Implementing the ME+PS merging algorithm", *JHEP* **07** (2005) 018, doi:10.1088/1126-6708/2005/07/018, arXiv:hep-ph/0503281.

[82] D. Reichelt, P. Richardson, and A. Siodmok, "Improving the simulation of quark and gluon jets with Herwig 7", *Eur. Phys. J. C* **77** (2017) 876, doi:10.1140/epjc/s10052-017-5374-8, arXiv:1708.01491.

[83] A. J. Larkoski, D. Neill, and J. Thaler, "Jet shapes with the broadening axis", *JHEP* **04** (2014) 017, doi:10.1007/JHEP04(2014)017, arXiv:1401.2158.

[84] J. R. Andersen et al., "Les Houches 2015: Physics at TeV colliders Standard Model working group report", in *9th Les Houches Workshop on Physics at TeV Colliders (PhysTeV 2015) Les Houches, France, June 1-19, 2015*. 2016. arXiv:1605.04692.

[85] E. Farhi, "Quantum chromodynamics test for jets", *Phys. Rev. Lett.* **39** (1977) 1587, doi:10.1103/PhysRevLett.39.1587.

[86] Y. L. Dokshitzer, G. D. Leder, S. Moretti, and B. R. Webber, "Better jet clustering algorithms", *JHEP* **08** (1997) 001, doi:10.1088/1126-6708/1997/08/001, arXiv:hep-ph/9707323.

[87] M. Dasgupta, A. Fregoso, S. Marzani, and G. P. Salam, "Towards an understanding of jet substructure", *JHEP* **09** (2013) 029, doi:10.1007/JHEP09(2013)029, arXiv:1307.0007.

[88] J. M. Butterworth, A. R. Davison, M. Rubin, and G. P. Salam, "Jet substructure as a new Higgs search channel at the LHC", *Phys. Rev. Lett.* **100** (2008) 242001, doi:10.1103/PhysRevLett.100.242001, arXiv:0802.2470.

[89] S. Schmitt, "TUnfold: an algorithm for correcting migration effects in high energy physics", *JINST* **7** (2012) T10003, doi:10.1088/1748-0221/7/10/T10003, arXiv:1205.6201.

[90] M. Cacciari et al., “The t anti-t cross-section at 1.8-TeV and 1.96-TeV: A study of the systematics due to parton densities and scale dependence”, *JHEP* **04** (2004) 068, doi:10.1088/1126-6708/2004/04/068, arXiv:hep-ph/0303085.

[91] S. Catani, D. de Florian, M. Grazzini, and P. Nason, “Soft gluon resummation for Higgs boson production at hadron colliders”, *JHEP* **07** (2003) 028, doi:10.1088/1126-6708/2003/07/028, arXiv:hep-ph/0306211.

[92] A. Hoecker et al., “TMVA - toolkit for multivariate data analysis”, *arXiv e-prints* (2007) physics/0703039, arXiv:physics/0703039.

A Plots for TWiki: Detector level distributions

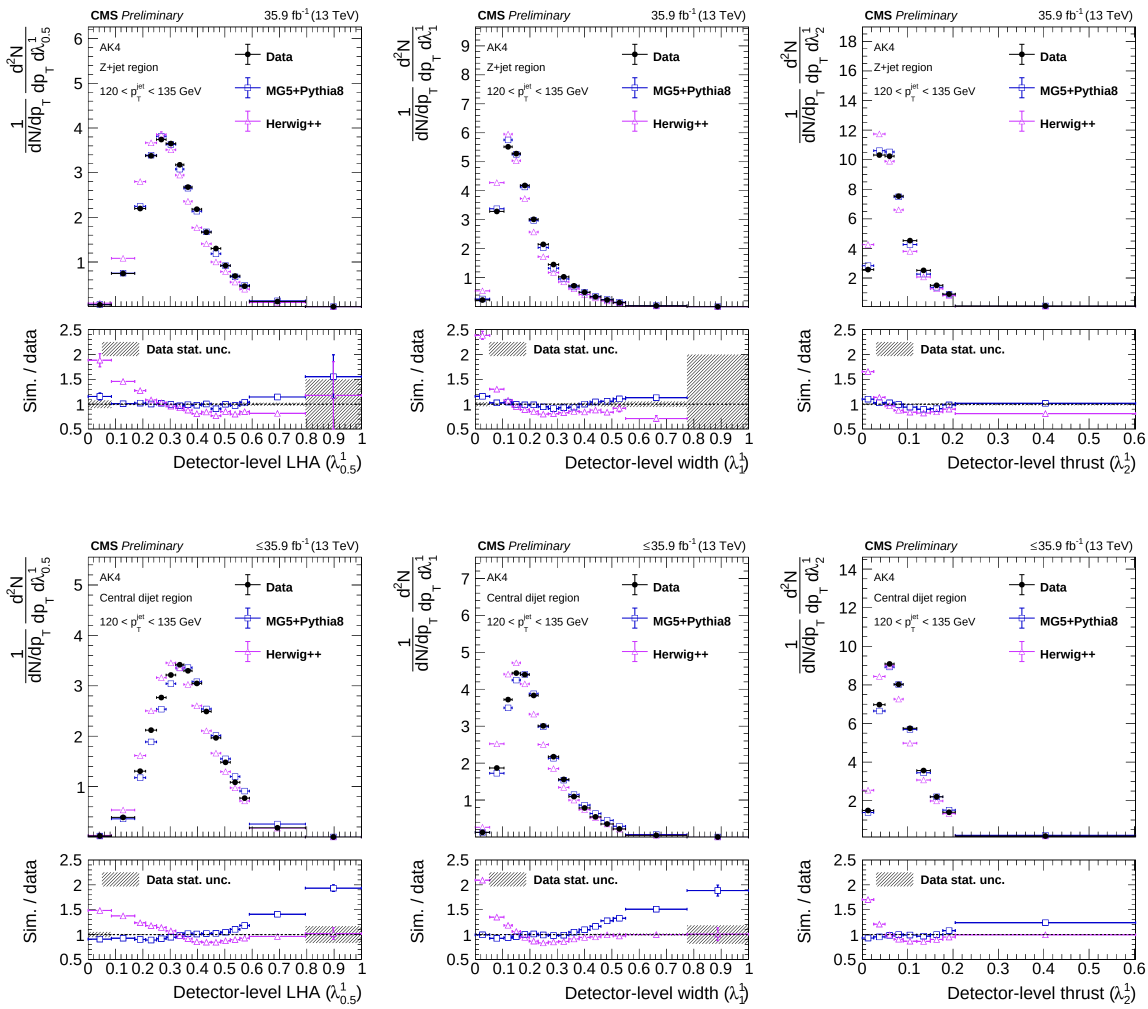

Figure 15: Data to simulation comparisons for substructure observables in $120 < p_{\mathrm{T}} < 150$ GeV in the Z+jet (upper) and central dijet regions (lower): LHA ($\lambda^1_{0.5}$), width (λ^1_1) and thrust (λ^1_2). The error bars and the hashed area in the ratio plot correspond to the statistical uncertainties of the data.

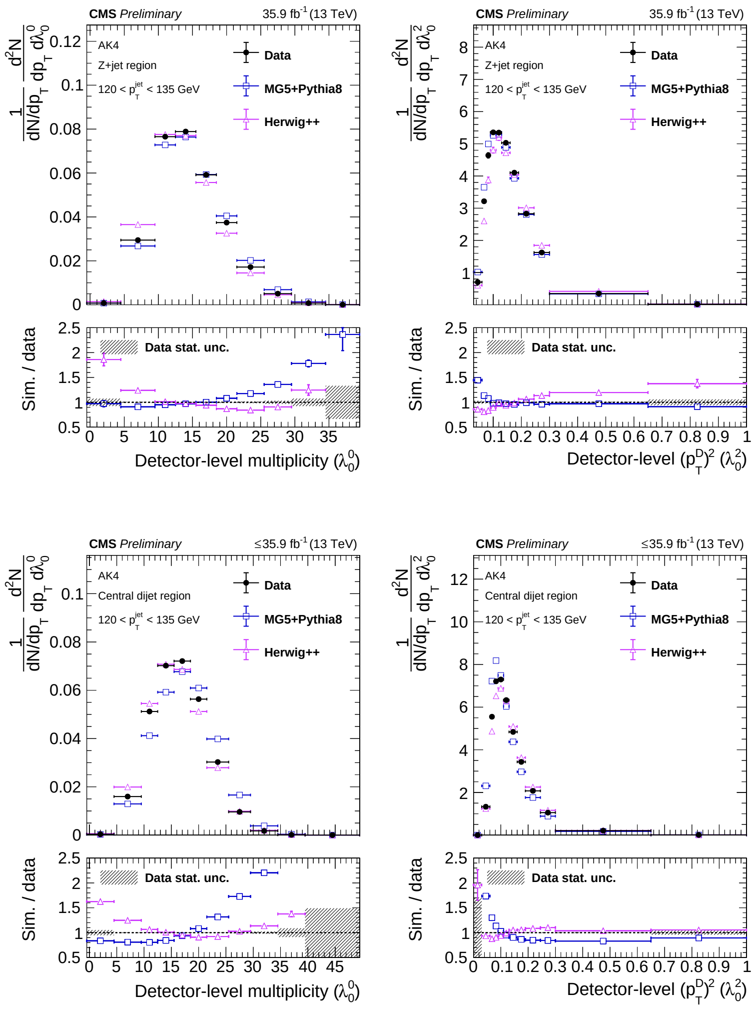

Figure 16: Data to simulation comparisons for substructure observables in $120 < p_{\mathrm{T}} < 150\,\mathrm{GeV}$ in the Z+jet (upper) and central dijet regions (lower): multiplicity, $(p_{\mathrm{T}}^{D})^{2}$ (λ_{0}^{2}). The error bars and the hashed area in the ratio plot correspond to the statistical uncertainties of the data.

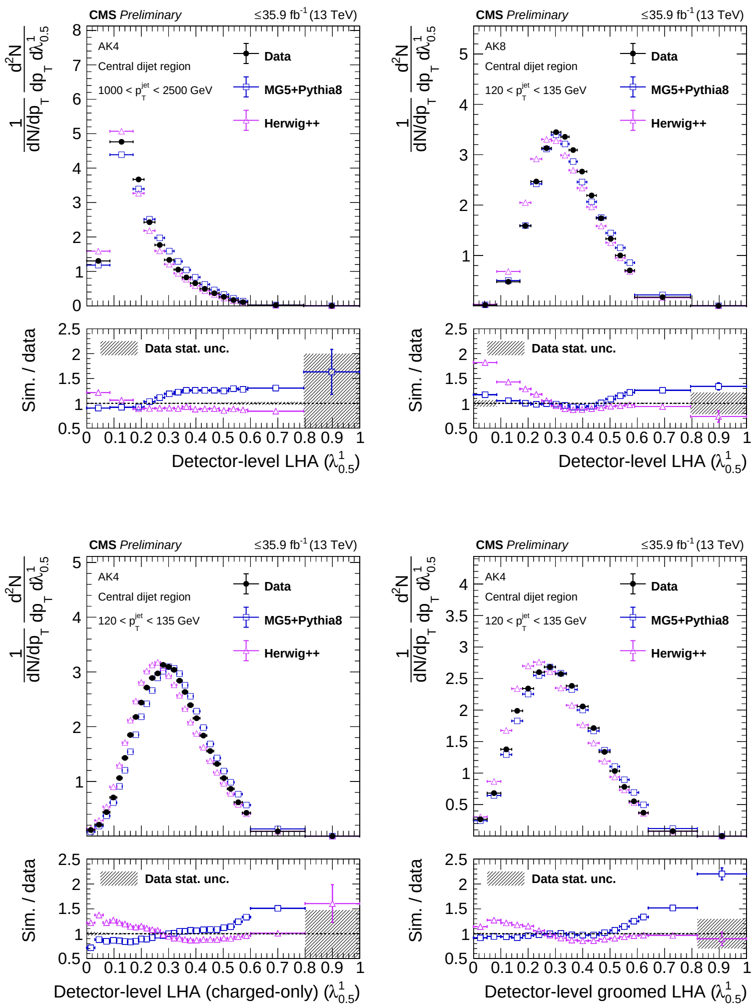

Figure 17: Data to simulation comparisons for variants of LHA ($\lambda^1_{0.5}$) in the central dijet region: (upper left) ungroomed AK4 $1000 < p_T < 1500$ GeV, (upper right) ungroomed AK8 $120 < p_T < 150$ GeV, (lower left) ungroomed charged-only AK4 $120 < p_T < 150$ GeV, (lower right) groomed AK4 $120 < p_T < 150$ GeV. The error bars and the hashed area in the ratio plot correspond to the statistical uncertainties of the data.

B Plots for TWiki: Delta summary

The figure of merit Δ, used by TMVA [92] to determine classifier separation, is a measure of the difference between two probability distributions, $p_1(\lambda), p_2(\lambda)$, defined as

$$\Delta = \frac{1}{2} \int \frac{[p_1(\lambda) - p_2(\lambda)]^2}{p_1(\lambda) + p_2(\lambda)} \, \mathrm{d}\lambda \tag{3}$$

with

$$\int p_i(\lambda) \, \mathrm{d}\lambda = 1, \tag{4}$$

where a value of $\Delta = 0$ indicates that the two distributions are identical, whilst $\Delta = 1$ indicates that the two distributions are completely different. A summary is shown in Fig. 18.

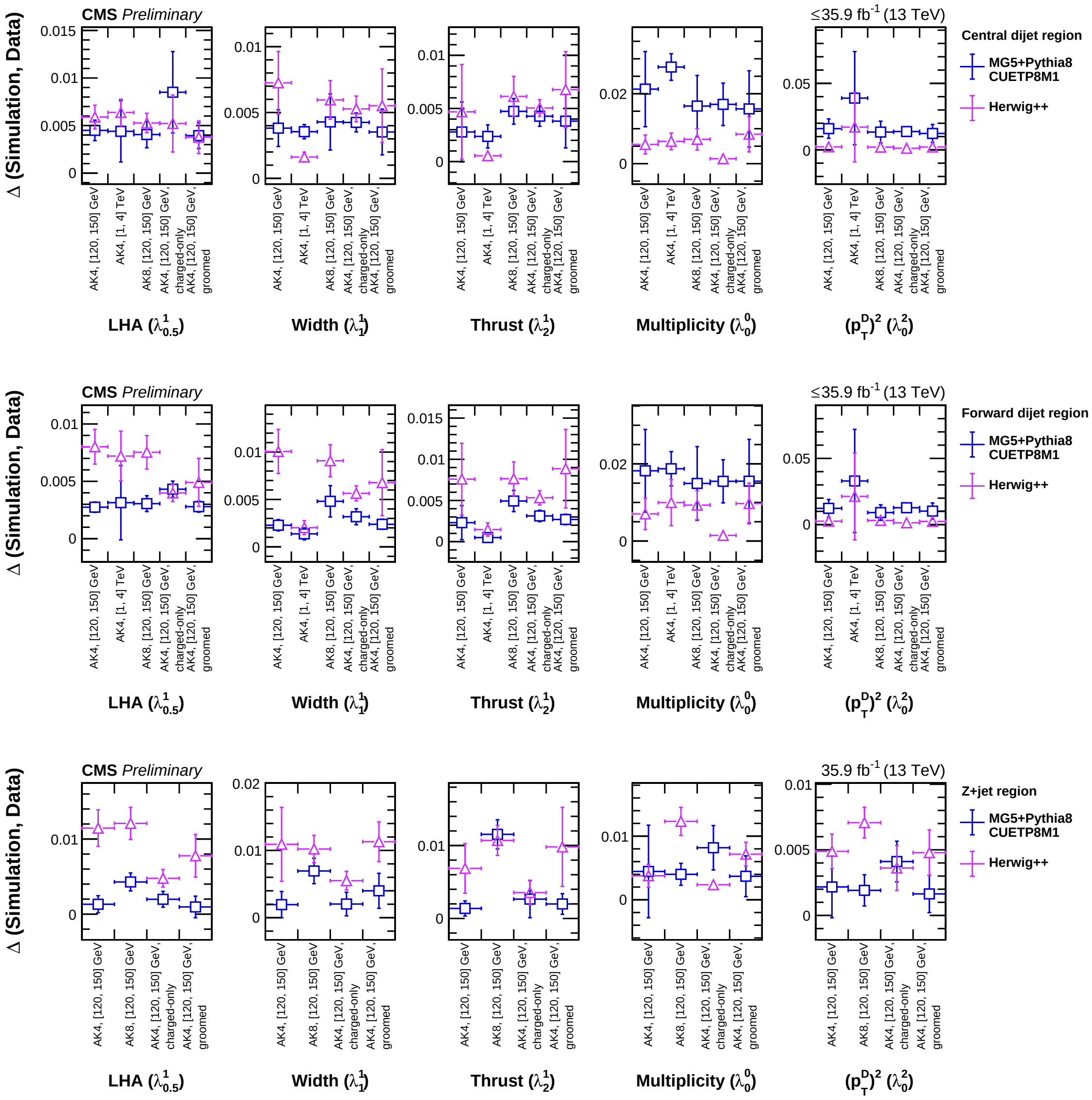

Figure 18: Δ of substructure observables in the central dijet (upper), forward dijet (middle) and Z+jet (lower) regions with the following entries on x-axis: ungroomed AK4 $120 < p_T < 150\,\text{GeV}$, ungroomed AK4 $1000 < p_T < 1500\,\text{GeV}$, ungroomed AK8 $120 < p_T < 150\,\text{GeV}$, ungroomed charged-only AK4 $120 < p_T < 150\,\text{GeV}$, groomed AK4 $120 < p_T < 150\,\text{GeV}$ for the observables multiplicity, LHA ($\lambda^1_{0.5}$), $(p_T^D)^2$ (λ^2_0), width (λ^1_1) and thrust (λ^1_2).

C Plots for TWiki: Mean, AK4 ungroomed jets

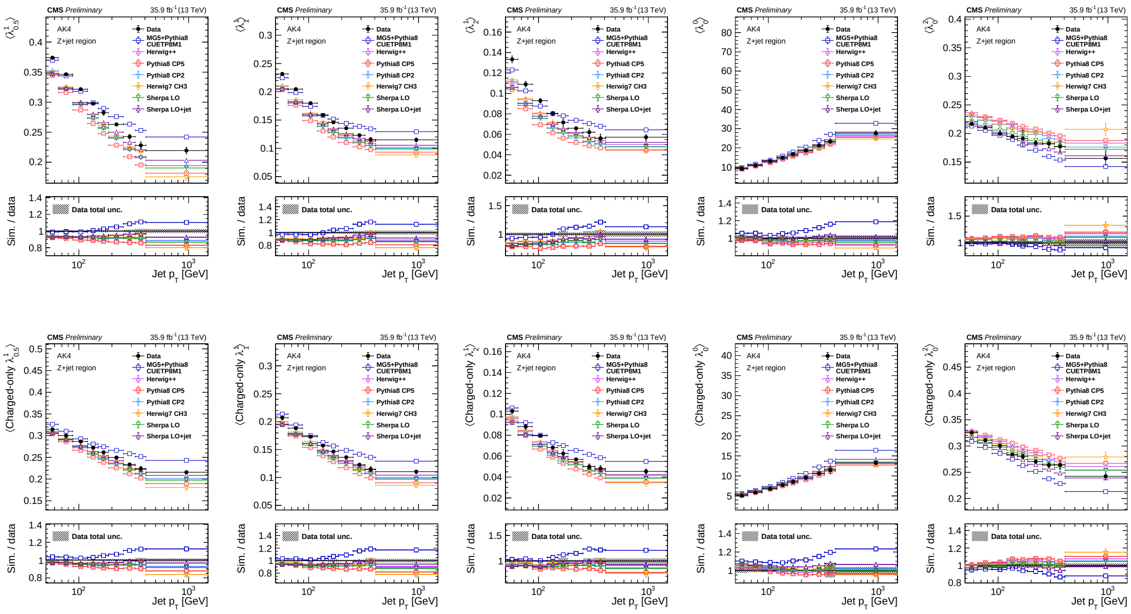

Figure 19: Plots of distribution mean for ungroomed AK4 jets in the Z+jet region, comparing unfolded data to MC. Upper row is charged+neutral variables, lower row is charged-only variables.

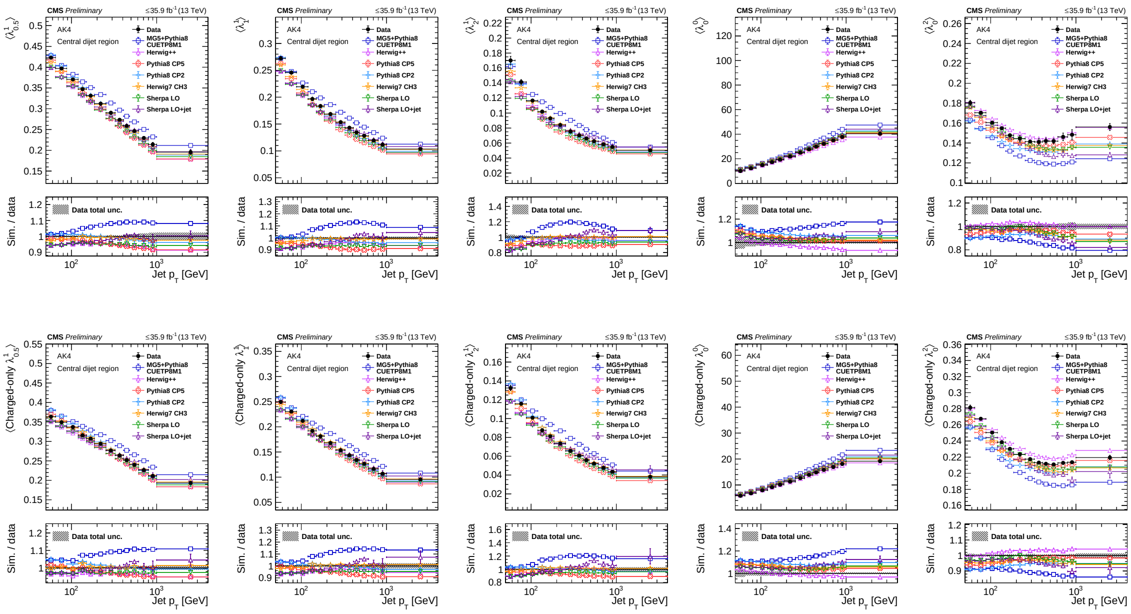

Figure 20: Plots of distribution mean for ungroomed AK4 jets in the central dijet region, comparing unfolded data to MC. Upper row is charged+neutral variables, lower row is charged-only variables.

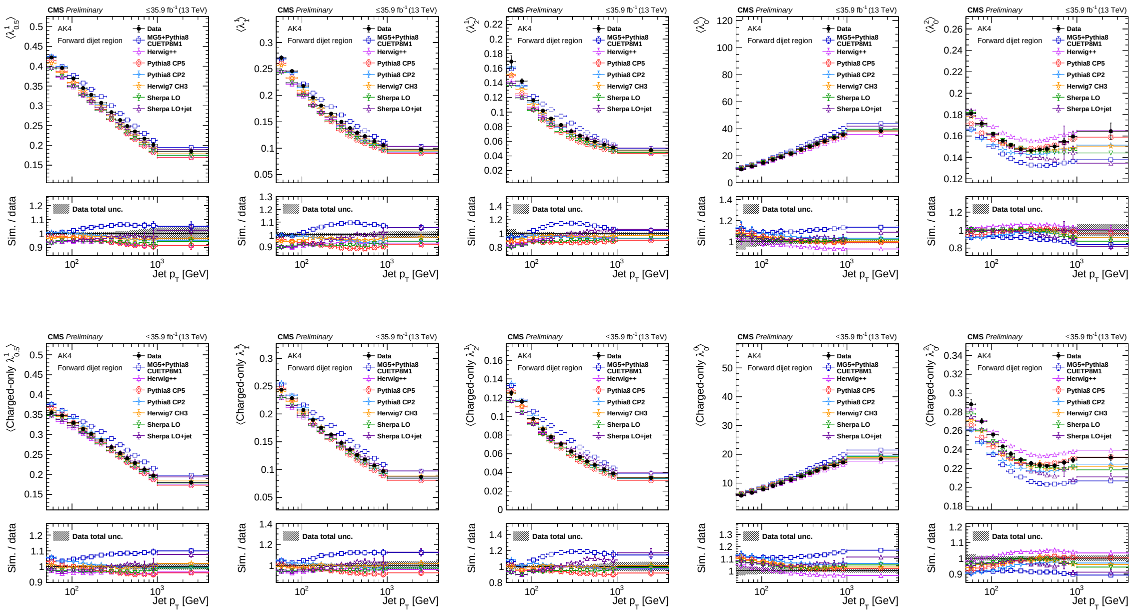

Figure 21: Plots of distribution mean for ungroomed AK4 jets in the forward dijet region, comparing unfolded data to MC. Upper row is charged+neutral variables, lower row is charged-only variables.

D Plots for TWiki: Mean, AK4 groomed jets

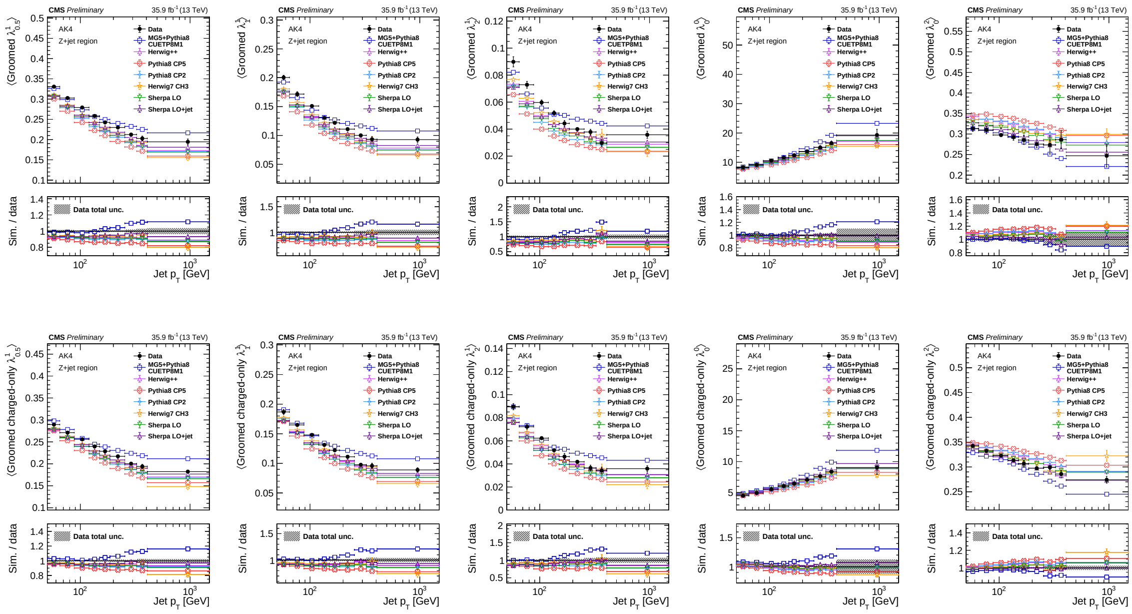

Figure 22: Plots of distribution mean for groomed AK4 jets in the Z+jet region, comparing unfolded data to MC. Upper row is charged+neutral variables, lower row is charged-only variables.

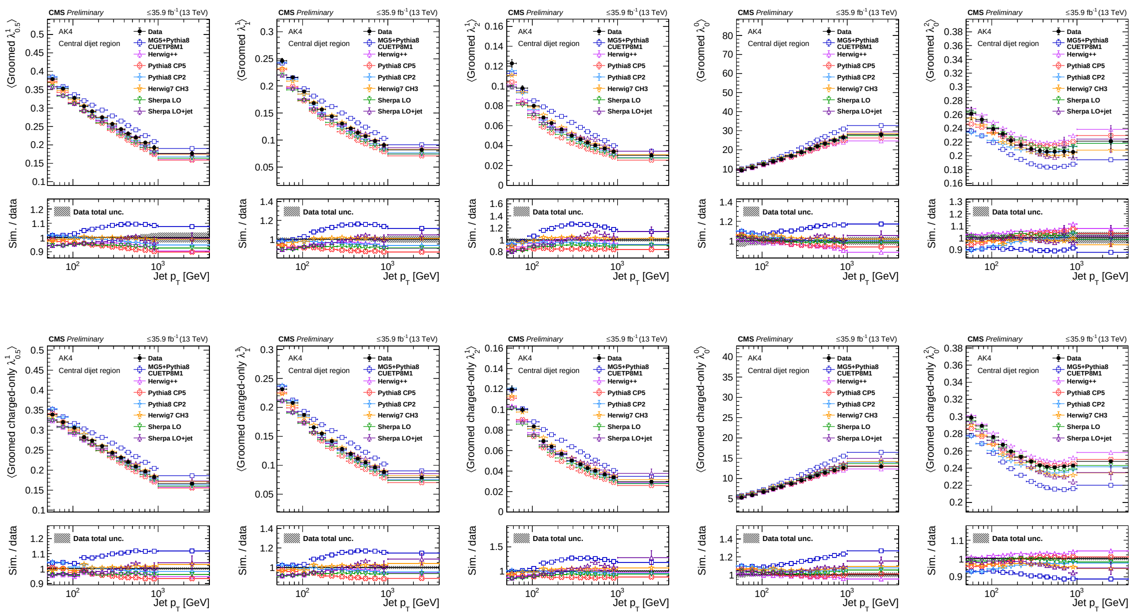

Figure 23: Plots of distribution mean for groomed AK4 jets in the central dijet region, comparing unfolded data to MC. Upper row is charged+neutral variables, lower row is charged-only variables.

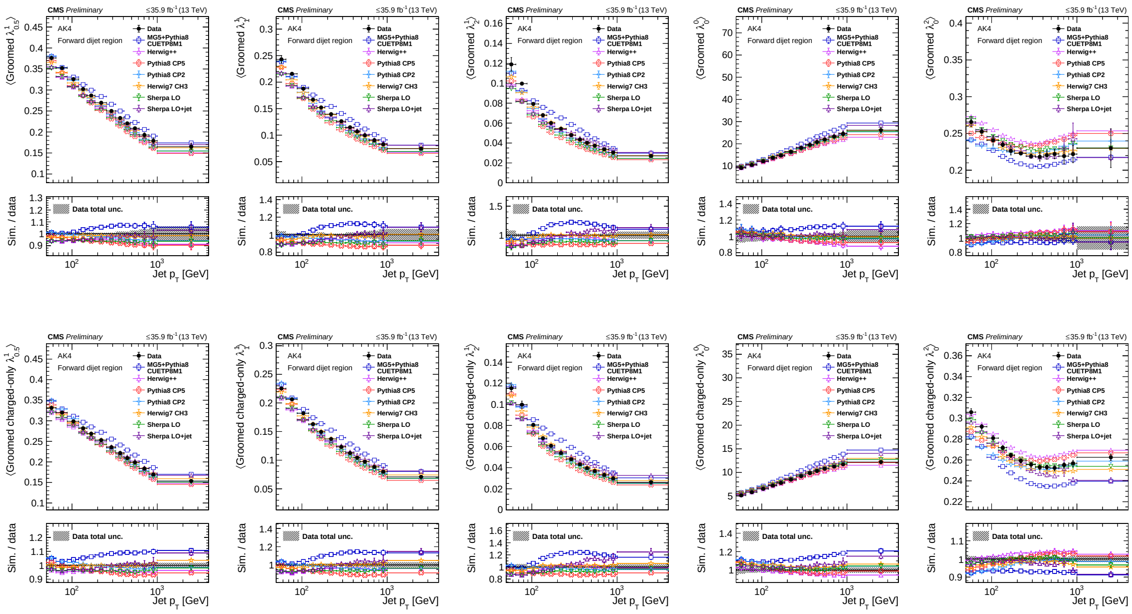

Figure 24: Plots of distribution mean for groomed AK4 jets in the forward dijet region, comparing unfolded data to MC. Upper row is charged+neutral variables, lower row is charged-only variables.

E Plots for TWiki: Mean, AK8 ungroomed jets

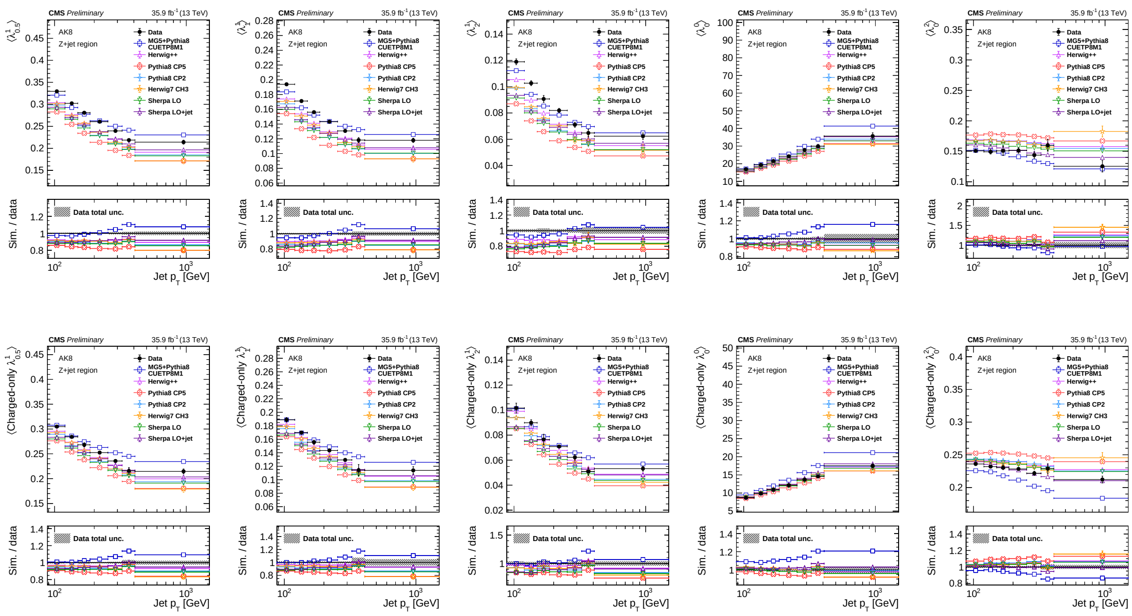

Figure 25: Plots of distribution mean for ungroomed AK8 jets in the Z+jet region, comparing unfolded data to MC. Upper row is charged+neutral variables, lower row is charged-only variables.

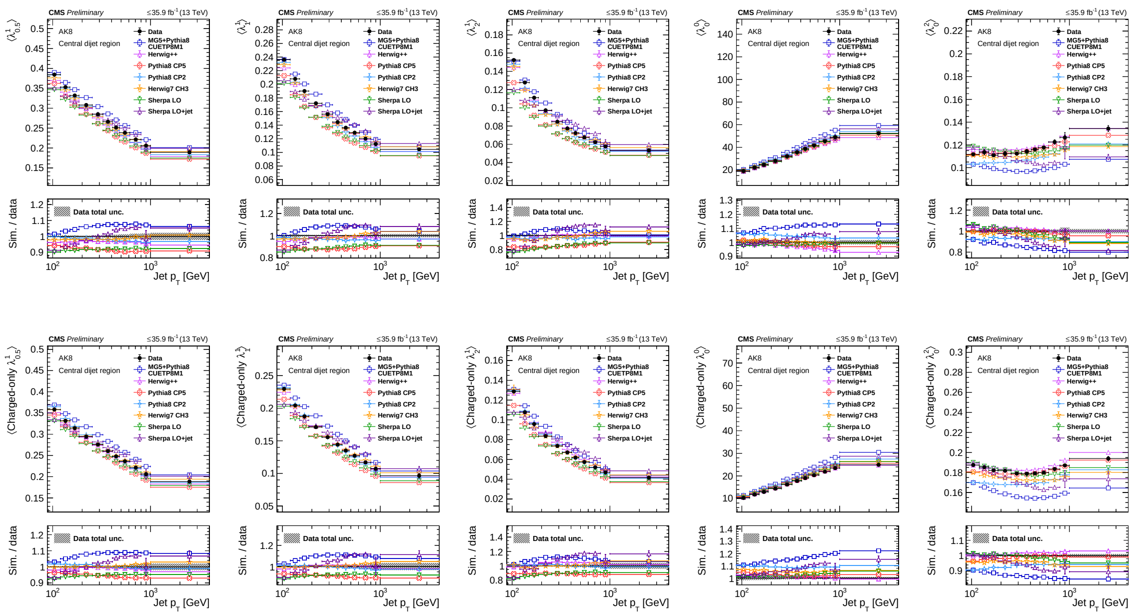

Figure 26: Plots of distribution mean for ungroomed AK8 jets in the central dijet region, comparing unfolded data to MC. Upper row is charged+neutral variables, lower row is charged-only variables.

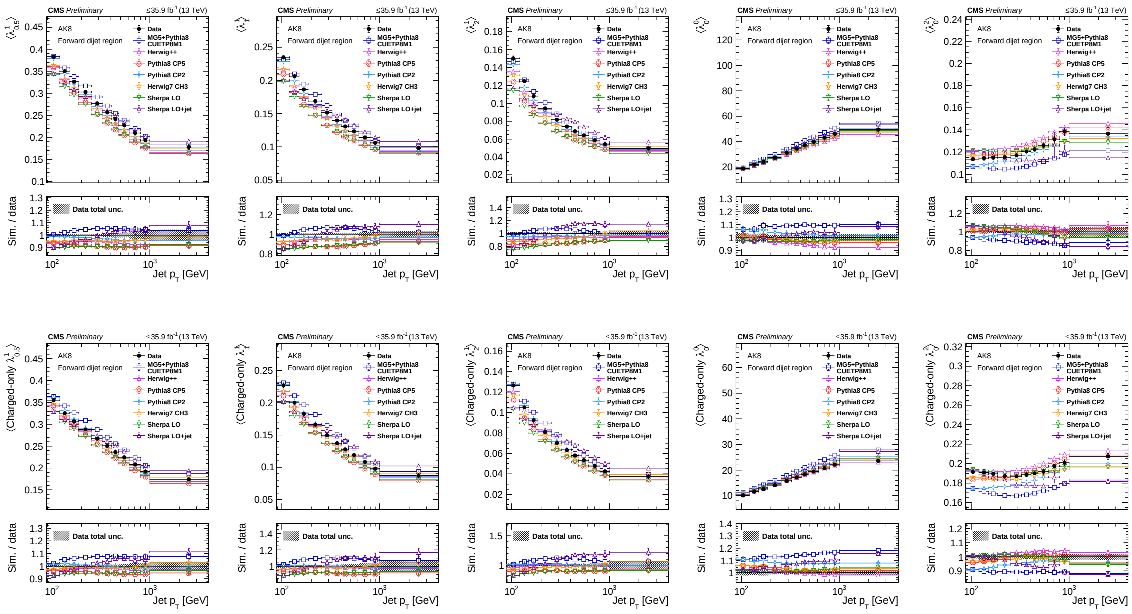

Figure 27: Plots of distribution mean for ungroomed AK8 jets in the forward dijet region, comparing unfolded data to MC. Upper row is charged+neutral variables, lower row is charged-only variables.

F Plots for TWiki: Mean, AK8 groomed jets

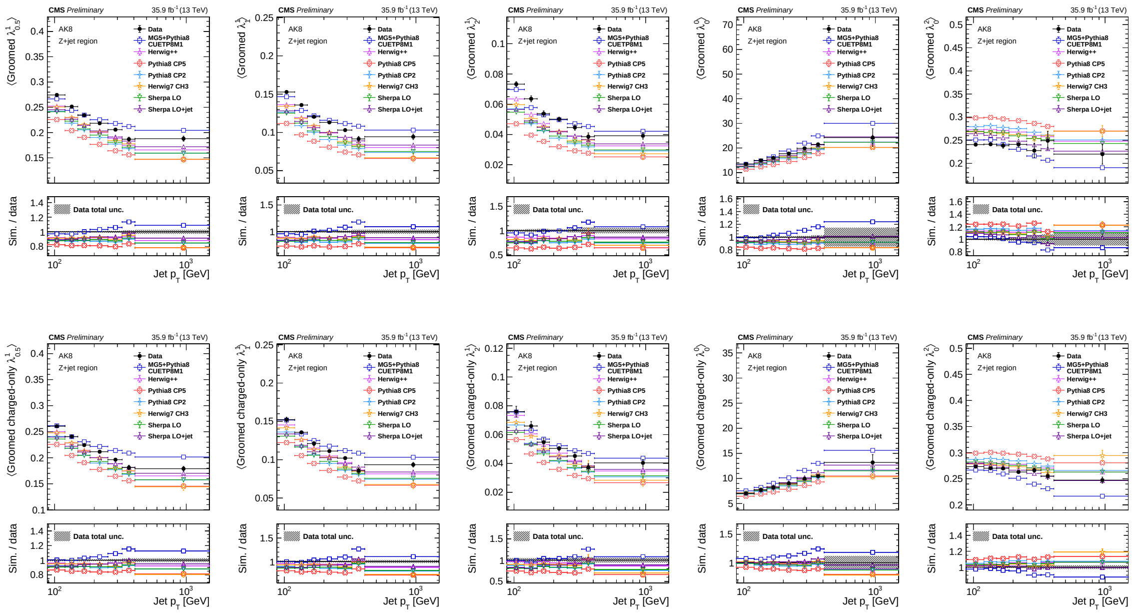

Figure 28: Plots of distribution mean for groomed AK8 jets in the Z+jet region, comparing unfolded data to MC. Upper row is charged+neutral variables, lower row is charged-only variables.

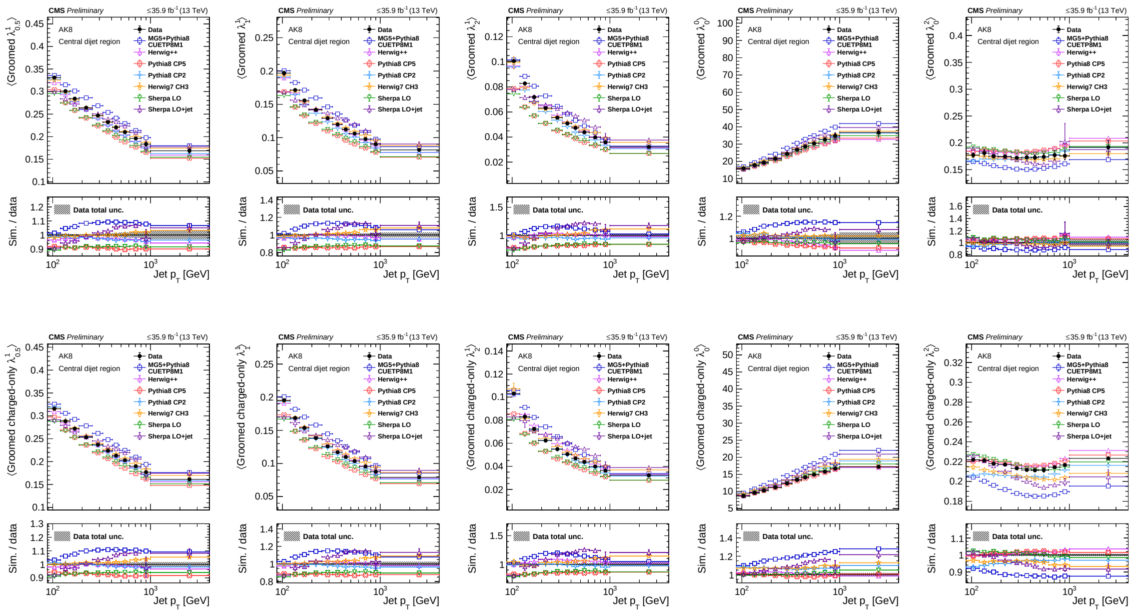

Figure 29: Plots of distribution mean for groomed AK8 jets in the central dijet region, comparing unfolded data to MC. Upper row is charged+neutral variables, lower row is charged-only variables.

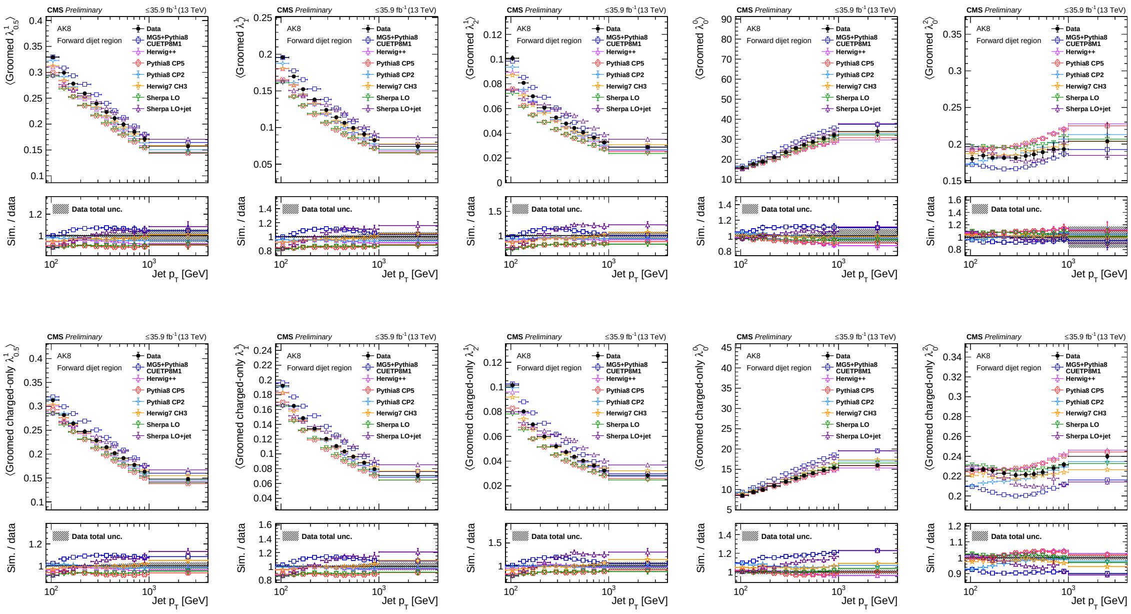

Figure 30: Plots of distribution mean for groomed AK8 jets in the forward dijet region, comparing unfolded data to MC. Upper row is charged+neutral variables, lower row is charged-only variables.

G Plots for TWiki: Flavour fractions

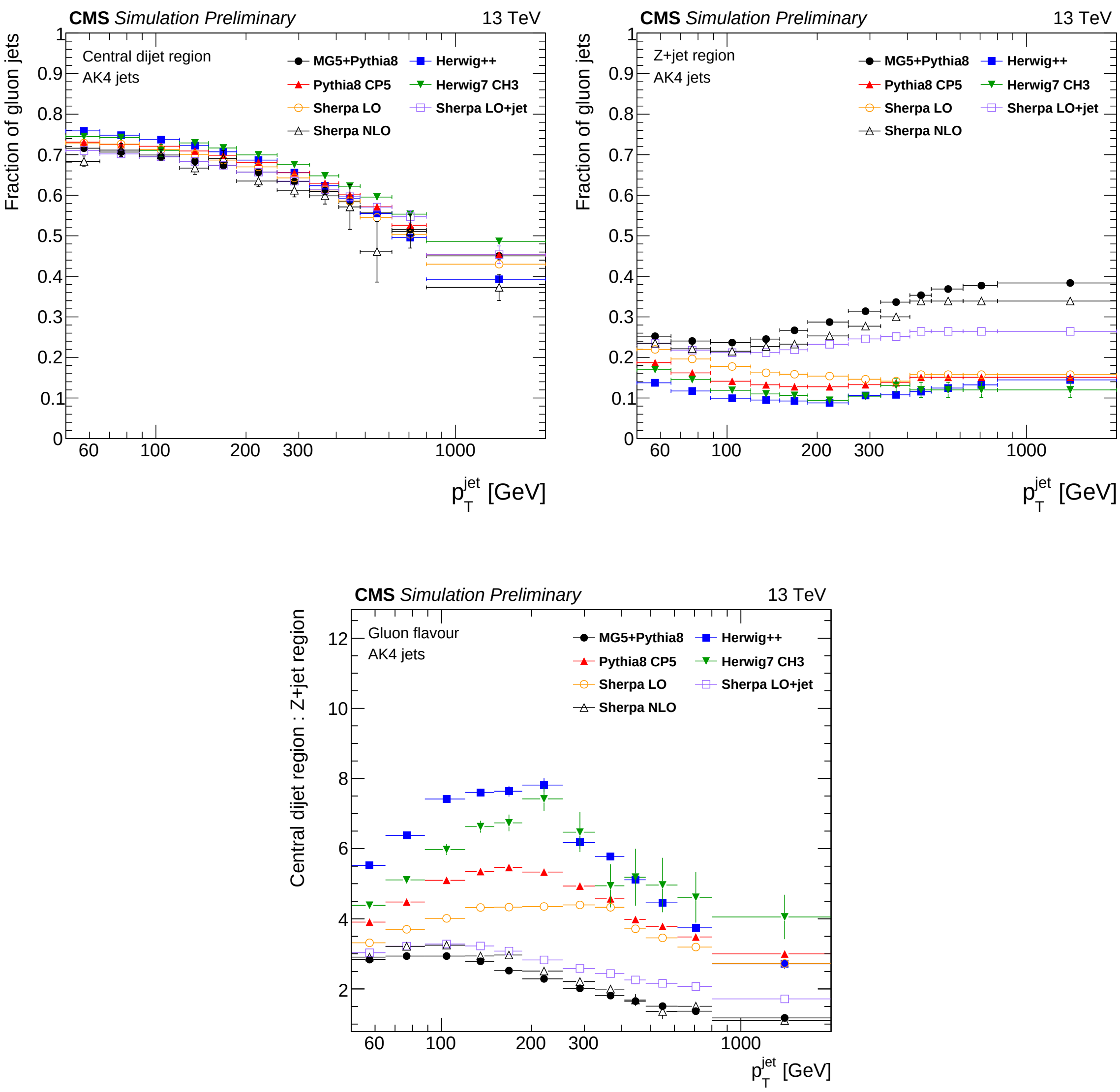

Figure 31: Upper left: gluon jet flavour fraction as a function of jet p_T in central dijet region for AK4 jets. Upper right: gluon jet flavour fraction as a function of jet p_T in Z+jet region for AK4 jets. Lower: ratio of gluon jet fraction in central dijet region to Z+jet region as a function of jet p_T for AK4 jets. SHERPA LO+jet is SHERPA LO with CKKW matching for up to 2 (1) additional outgoing partons for the dijet (Z+jet) processes.